Research Square

Preprints are preliminary reports that have not undergone peer review.
They should not be considered conclusive, used to inform clinical practice,
or referenced by the media as validated information.

# Donor Age Impairs Vasculogenic Potential of hiPSC-Derived Endothelial Progenitors via Elevated Mitochondrial Reactive Oxygen Species

**Bryce Larsen**
The University of Texas at Austin
**Cody Callahan**
The University of Texas at Austin
**Arshitha Rayanki**
The University of Texas at Austin
**Anna McClain**
The University of Texas at Austin
**Weixuan Wu**
The University of Texas at Austin
**Sara Faulkner**
The University of Texas at Austin
**Janet Zoldan**
z.janet@utexas.edu

The University of Texas at Austin

**Article**

**Keywords:**

**Posted Date:** September 23rd, 2026

**DOI:** https://doi.org/10.21203/rs.3.rs-10899210/v1

**License:** This work is licensed under a Creative Commons Attribution 4.0 International License.
Read Full License

**Additional Declarations:** No competing interests reported.

# Abstract

Background:

Human induced pluripotent stem cells (hiPSCs) are a promising source for autologous vascular regeneration, but preliminary research often relies on neonatal donors, whereas clinical applications will use cells derived from aged individuals. Although the impact of donor age on reprogramming efficiency and hiPSC characteristics has been studied, the effect on the functionality of $CD34^+$ hiPSC-derived endothelial progenitors (hiPSC-EPs) remains understudied.

To investigate potential differences, we differentiated EPs from hiPSCs derived from three neonatal donors (ND) and three mature donors (MD) with sex- and somatic cell origin-matching between lines. This comparison revealed donor age-associated, phenotypical, functional, epigenetic, and transcriptomic differences. Notably, when cultured in 3D hydrogels, all MD-hiPSC-EPs showed markedly reduced vasculogenic potential relative to ND-hiPSC-EPs, forming vascular structures that were poorly interconnected and largely non-lumenized.

DNA methylation profiling revealed that somatic cell origin was the dominant driver of variance, however, key donor age-associated differences were also present. MD-hiPSCs were hypomethylated compared to their matched pairs and we observed differentially methylated regions associated with mesoderm commitment, angiogenesis, ECM remodeling, cytoskeleton-organization and mitochondria regulation. Specifically in mitochondrial regulation genes, we found a decrease in the methylation of canonical mitochondrial reactive oxygen species (ROS) associated genes in MD-hiPSC-EPs. RNA-sequencing further highlighted a donor age-associated shift in mitochondrial regulation with a clear donor age-dependent separation in the Mitochondrial Gene Regulation pathway. We further examined mitochondrial function in a representative ND-hiPSC and MD-hiPSC pair and found that MD-hiPSC-EPs exhibited a decrease in mitochondrial membrane potential concurrent with an increase in mitochondrial ROS (mtROS).

To investigate whether increased mtROS in MD-hiPSCs detrimentally impacted their functionality, we treated MD-hiPSCs with an mtROS-specific antioxidant. Once treated, we observed a shift to an ND-hiPSC-EP like state.  We observed treated MD-hiPSC-EPs producing phenotypical similarities, shared methylation changes, transcriptomic grouping, and improvement in network formation, achieving levels observed in ND-hiPSC-EPs.

These findings underscore the necessity of donor-specific considerations in hiPSC-based vascular engineering and highlight potential barriers and solutions to translating autologous hiPSC-derived therapeutics into aged patient populations.


# Introduction

Cardiovascular diseases remain the leading cause of mortality worldwide and are especially prevalent in the United States (1, 2). While several risk factors are lifestyle-dependent, aging stands out as a significant and unavoidable contributor (3). Some of the prominent age-related changes driving cardiovascular disease include a decline in vascular density and function. In aged individuals, studies show rarefaction of the microvasculature in multiple organs, including the heart (4). This loss, combined with a diminished regenerative capacity in aged tissues, is a critical challenge for current therapies which do not fully restore or replace damaged and lost vasculature.

Given these challenges, engineering replacement tissues offers a promising strategy for treating cardiovascular disease in older patients. One such approach involves generating new vascular tissue using human induced pluripotent stem cells (hiPSCs) (5). Derived from somatic cells, hiPSCs are patient-specific and function similarly to embryonic stem cells with the ability to self-renew and differentiate into a wide array of cell types, including into multipotent endothelial progenitors (hiPSC-EPs) (6). Importantly, hiPSC-EPs can differentiate into the two main types of vascular cells, endothelial cells (ECs) and smooth muscle cells (SMCs). Uniquely, they are capable of self-assembly into lumen containing networks in 3D culture without additional stromal cell support (7). This differentiation capacity makes hiPSC-EPs a valuable tool for studying and potentially replacing or regenerating damaged vasculature. Their patient specificity also opens avenues for personalized preclinical models and therapies.

While this patient specificity offers significant advantages, it also introduces variability based on the characteristics of the donor cell. For instance, somatic cell origin has been shown to influence hiPSCs' differentiation propensity to endothelial progenitor cells (hiPSC-EPs) (8). While somatic cell origin has been considered, the impact of hiPSC donor age on hiPSC-EP functionality remains largely unexplored. Most existing work on the impact of donor age on differentiated hiPSCs has primarily focused on differentiation propensity, without quantitatively investigating how age-related factors affect downstream functionality (9). This gap in understanding how donor background impacts functionality presents a critical barrier to translating hiPSC-based vascular therapies into clinical settings.

Furthermore, current hiPSC-derived vascular engineering relies heavily on somatic cells obtained from newborn or fetal donors (10–15). While neonate donor-hiPSCs (ND-hiPSCs) are useful in a research setting, they do not accurately represent the cells derived from the patient population who are most likely to benefit from hiPSC-derived vascular therapies. Cardiovascular disease incidence is rare in neonates, but age-related vascular disease affects over 70% of individuals older than 60 (16). With recent evidence indicating hiPSCs from older donors exhibit distinct features, including increased methylation of genes associated with angiogenesis, it remains unclear whether findings obtained from ND-hiPSC-EPs will translate to hiPSC-EPs generated from, and ultimately intended for use in, mature patients (MD-hiPSCs) (17).

To address this critical knowledge gap, we characterized intrinsic differences between ND-hiPSC-EPs and MD-hiPSC-EPs and compared their functionality in *de novo* network formation using our *in vitro* vasculogenesis hydrogel platform. We have previously shown that iPSC-EPs encapsulated in these

hydrogels form robust, lumenized microvascular networks within one week and remain stable for over two weeks. A key advantage of this system is that iPSC-EPs self-assemble into vascular networks without the addition of supporting stromal cells, enabling more direct investigation vasculogenesis (7, 11, 18, 19)

We hypothesized that due to age-associated differences in methylation patterns, donor age would significantly influence the vasculogenic potential and cellular function of hiPSC-EPs. Although we didn't observe all of the specific methylation and gene expression trends reported by Lo Sardo et al. (17), we did find additional differences that resulted in functional impairment in MD-hiPSC-EPs. ND-hiPSC-EPs exhibited significantly greater vasculogenic potential, forming denser and more interconnected vascular networks in 3D environments compared to MD-hiPSC-EPs. Furthermore, MD-hiPSCs showed a higher EP yield, a decrease in cellular density, an increase in perinuclear VE-Cadherin in 2D culture, and distinct methylation and gene expression profiles. Across methylation and transcriptomic data, we noted differences in mitochondrial gene regulation, noting enrichment of mitochondrial reactive oxygen species handling genes. Consistent with the insights from RNA sequencing and methylation data, we found higher levels of mtROS and lower levels of mitochondrial membrane potential in MD-hiPSC-EPs. Notably, treatment with mtROS-specific antioxidant at the hiPSC stage shifted both epigenetic and phenotypic signatures to match ND-hiPSC-EPs and significantly restored network formation in MD-hiPSC-EPs to that of ND-hiPSC-EPs. Together, our findings demonstrate that donor age significantly impairs hiPSC-EP function and implicate elevated mtROS as a key mechanistic driver of this dysfunction.

# Materials and Methods

**Cell Lines and Culture**: We chose six human induced pluripotent stem cell (hiPSC) lines to use in this study, 3 from neonate donors and 3 from mature donors. Neonate donor age was under 1 week at the time of sampling, while mature donor age was 30 years or older. The hiPSC lines from neonate donors included: iPS-DF19-9-11T.H, designated as neonate donor 1 (ND-1) (WiCell, Cellosaurus ID: CVCL_K054); WISCi007-C, designated as neonate donor 2 (ND-2) (WiCell, Cellosaurus ID: CVCL_VF54); and CBhiPSC6.2, designated as neonate donor 3 (ND-3) (Thermo Fisher, Cat# A18945, Cellosaurus ID: CVCL_RM92). The hiPSC lines from mature donors included: WTC11, designated as mature donor 1 (MD-1) (UCSFi001-A, Cellosaurus ID: CVCL_Y803); WTB, designated as mature donor 2 (MD-2) (Gladstone WTB hiPSC line); and EDi044-A, designated as mature donor 3 (MD-3) (Cellosaurus ID: CVCL_YB36). ND-1, ND-2, MD-1, and MD-2 were derived from skin fibroblasts, while ND-3 and MD-3 were derived from $CD34^+$ mononuclear blood cells. ND-1 and MD-1 are both derived from male donors and ND-2,3 and MD-2,3 are derived from female donors (Fig. 1).

All hiPSC lines were cultured on vitronectin-coated plates (Thermo Fisher) and maintained in Essential 8 (E8) medium (Thermo Fisher). Plates were coated with vitronectin according to the manufacturer's protocol, using a 0.5 µg/mL solution prepared in Dulbecco's phosphate-buffered saline (DPBS) and incubated at 37°C for 1 hour prior to hiPSC seeding. hiPSCs were colony passaged every 3–4 days at approximately 70–80% confluency using 0.5 mM Ethylenediaminetetraacetic acid (EDTA) in DPBS

(Thermo Fisher). For routine culture, E8 medium was replaced daily. All cultures were maintained at 37°C in a humidified incubator with 5% $CO_2$.

**Endothelial Progenitor Differentiation**

We adapted and optimized the differentiation protocol from Jalilian et al. to generate endothelial progenitors (EPs) from induced pluripotent stem cells (hiPSCs) (19, 20). After culturing hiPSCs as described above, we dissociated them into a single-cell suspension using Accutase (Innovative Cell Technologies) and plated them at a density of 10,000 cells/cm² on Geltrex-coated plates (Thermo Fisher) in Complete E8 medium supplemented with 10 μM Y-27632 (Selleck Chemicals).

One day after seeding, we replaced the media with Complete E8 without Y-27632. Two days after seeding, we replaced the media with differentiation-inducing media, consisting of Dulbecco's Modified Eagle Medium Nutrient Mixture F-12 (DMEM-F12) (Cytiva) supplemented with N2 supplement (Thermo Fisher) and B27 without insulin (Thermo Fisher), along with 25 ng/mL Activin A (R&D Systems), 30 ng/mL Bone Morphogenic Protein 4 (BMP4, R&D Systems), and 0.15 μM 6-bromoindirubin-3-oxime (BIO, Selleck Chemicals). After an additional day, we replaced the differentiation media with fresh differentiation media supplemented with Activin A, BMP4, and BIO at the above concentrations.

Four days after seeding, we replaced the media with differentiation media supplemented with 2 μM SB431542 (Tocris) and 50 ng/mL Vascular Endothelial Growth Factor (VEGF, ACRO **Biosystems). We continued replenishing this media daily for two additional days.**

**Isolation and Characterization of hiPSC-EPs Using Flow Cytometry**: Seven days after seeding, $CD34^+$ hiPSC-EPs were isolated as follows. We incubated the differentiated cells with Accutase (STEMCELL Technologies) for 10 minutes at 37°C and dissociated them into single cells. After centrifuging at 300g for 5 minutes, we resuspended the resulting pellet in 200 μL of sorting buffer (2 mM EDTA, 0.5% bovine serum albumin in DPBS; Sigma-Aldrich). At this stage, cells were either used for $CD34^+$ cell isolation or further characterized by flow cytometry.

For $CD34^+$ cell isolation, cells were stained with a 1:50 dilution of CD34-FITC antibody (Miltenyi Biotec) for 10 minutes at 4°C. Prior sorting, cells were filtered three times through a 35 μm cell strainer (Corning) to remove cell and extracellular matrix aggregates. $CD34^+$ hiPSC-EPs were isolated, by fluorescence-activated cell sorting (FACS) (S3e; Bio-Rad). We determined $CD34^+$ yield using population analysis tools from ProSort, the Bio-Rad software native to the S3e cell sorter, and FlowJo.

For phenotypic characterization, cells were stained for 30 min at 4°C with the following antibodies at 1:50 dilution: CD45-VioBlue (Miltenyi, 130-110-775), CD34-FITC (Miltenyi, 130-113-178), CD31-APC (Miltenyi, 130-110-670), CD140a-AF700 (Miltenyi, 130-132-015), CD140b- APC-Vio770 (Miltenyi, 130-129-455). Samples were analyzed using a Sony MA900 flow cytometer and data were processed in FlowJo.

**Formulation of hiPSC-EP-laden hydrogels**

We encapsulated hiPSC-EPs in collagen/norbornene-modified hyaluronic acid (NorHA) hydrogels using methods described previously by our group (7, 19). We chose collagen NorHA hydrogels because of their tunable stiffness, cell affinity, and degradation properties allowing for optimized controlled vasculogenic conditions. Based on previous studies done by our group, we chose a cell density of 2.2 million cells/ml, a collagen density of 2.5 mg/ml, and a 25% crosslinking of the available norbornene groups between hyaluronic acid chains.

Shortly after sorting, we centrifuged the hiPSC-EPs at 300 g for 5 minutes and then resuspended them in endothelial growth media 2 (EGM2; PromoCell Inc), supplemented with 10 μM Y-27632 and 1X Antibiotic Antimycotic (Sigma-Aldrich). We embedded the resuspended hiPSC-EPs in the Collagen/NorHA hydrogels as previously described (7, 19). Briefly, we mixed 10X Medium 199 (ThermoFisher Scientific) with type 1 rat tail collagen dissolved in acetic acid (Corning) and neutralized the solution with 1 M sodium hydroxide (Sigma-Aldrich). We then added this solution to a mixture of NorHA, RGD (GCGYGRGDSPG) (2.06 mg/ml), and an enzymatically degradable peptide (KCGPQGIWGQCK) (2.21 mg/ml). Finally, lithium phenyl-2,4,6-trimethylbenzoylphosphinate (LAP) was incorporated into a final concentration of 0.025 wt% and served as the photo-initiator to crosslink the NorHA.

Next, we pipetted 50 μL of the neutralized collagen-NorHA-cell suspension into individual wells in an 18-well glass chamber slide (Ibidi) and allowed them to solidify for 30 minutes at 37°C and 5% $CO_2$. We then exposed the hydrogels to 365 nm light at 10 mW/cm² for 50 seconds (Omnicure Series 1500). The final hydrogels contained 1 wt% NorHA and 0.25 wt% collagen. Immediately after exposure to UV light, cell laden hydrogels were cultured in 100 μL of EGM2 supplemented with 50 ng/mL VEGF, 10 μM Y-27632, and 1X Antibiotic Antimycotic. We replaced media daily for 7 days, using 100 μL EGM2 supplemented with 50 ng/mL VEGF.

**Network Analysis**

We visualized the vessel-like networks generated within the hydrogels by fixing the hydrogels in 4% paraformaldehyde (PFA) 7 days after formulation and staining with rhodamine-phalloidin (ThermoFisher Scientific). For network quantification, we acquired Z-stacks at 10 μm intervals on a laser scanning confocal with a 10x objective (Leica SP8). At least 4 regions of interest across the full depth, between 500 and 800 μm, of the hydrogel were acquired per hydrogel sample, and at least three hydrogels were analyzed per experimental condition for a minimum of 12 per condition.

To analyze the total length, connectivity, and vessel diameter of the networks, we used a computational pipeline previously developed and described by our group (11). Briefly, we filtered and binarized confocal z-stacks of regions of interest of the hydrogel using ImageJ and then analyzed the stacks using a MATLAB script that converts the images into a nodal graph. This nodal graph was then used to determine the associated parameters of the capillary-like networks by analyzing the nodes (branch/endpoints) and links (vessels).

**2D Cell Culture**

hiPSC-EPs from all lines immediately after sorting were plated on vitronectin (0.5 µg/mL in DPBS) coated plates at 35,000 cells/$cm^2$ and cultured in EGM2 with the initial seeding media supplemented with 10 µM Y-27632 and 1X Antibiotic Antimycotic. We replaced the media with fresh EGM2 daily for 7 days. After 7 days the cells were fixed using 4% PFA and stained with either anti-VE-Cadherin at 1 µg/ml (Santa Cruz Biotechnology), and 4',6-diamidino-2-phenylindole (DAPI) 1 µg/ml (R&D Systems), or ant-CD31-FITC (Thermo Fisher) at 0.65 µg/mL and 4',6-diamidino-2-phenylindole (DAPI) 1 µg/ml (R&D Systems) which are the recommended concentrations from the suppliers. Samples were imaged using a laser scanning confocal (Leica SP8). At least 4 regions of interest per well were imaged at random and at least 4 wells per cell line were imaged.

VE-Cadherin images were analyzed using a custom Fiji/ImageJ macro that segmented nuclei from the DAPI channel, generated a 5-pixel-wide perinuclear ring around each nucleus, and measured VE-Cadherin intensity within this ring after background subtraction.

CD31 images were analyzed using a separate Fiji/ImageJ macro that thresholded the CD31 channel to define membrane rings, filled these rings to generate cell territory masks, and classified $DAPI^+$ nuclei as CD31-positive if their centroid fell within the mask territory, yielding the total nuclei count and CD31-positive count

**Senescence Analysis**

hiPSC-EPs from all lines immediately after sorting were plated on vitronectin (0.5 µg/mL in DPBS) coated plates at 35,000 cells/$cm^2$ and cultured in EGM2 with the initial seeding media supplemented with 10 µM Y-27632 and 1X Antibiotic Antimycotic. We replaced the media with fresh EGM2 daily for 7 days. A subset of hiPSC-EPs were cultured with Palbociclib (Thermo Fisher) at 1 µM for the full 7 days. hiPSC-EPs from both standard culture and palbociclib treated (positive control, known to induce cell senescence (21) conditions were fixed on days 3, 5 and 7 of culture and assessed for expression of β-galactosidase (β-gal), a cell senescence marker, using the CellEvent™ Senescence Green Detection Kit (Thermo Fisher).

**Epigenetic Analysis**: We collected between 500,000 and 1,000,000 $CD34^+$ cells immediately after sorting and extracted genomic DNA using the PureLink™ Genomic DNA Mini Kit (Thermo Fisher) by following the manufacturer's guidelines. Extracted and purified genomic DNA concentration was quantified using a Take3 and Cytation 3, then submitted to the University of Texas at Austin Genomic Sequencing and Analysis Core Facility (RRID:SCR_021713), which supplied us with the raw .idat files generated from the EPICv2 methylation assay (Illumina). All analyses were conducted in R Studio using standard workflows as described in the EPICv2 tutorial (22). IDAT files containing raw signal intensities were processed using the Sesame package in R for preprocessing and normalization (23). Initial quality control steps included assessing sample and probe-level metrics to remove low-quality or failed probes, background correction, and dye-bias normalization. ß values were extracted to quantify DNA methylation levels. Additional probe filtering was conducted to exclude SNP-overlapping and cross-reactive probes as well

as to remove probes that were matched to sex chromosomes. Age prediction was performed using the predictAge function within Sesame, applying the Horvath skin and blood algorithm (24). Gestational age was predicted using the Knight algorithm and the methylclock package in R Studio (25, 26). Discovery of differently methylated regions was done using the DMRcate package and recommended thresholds (27).

**RNA seq**: Total RNA was collected from separate differentiations, purified with RNeasy Mini Kit (Qiagen) according to the manufacturer's protocol, and submitted to the University of Texas Genomic Sequencing and Analysis Facility (Center for Biomedical Research Support, RRID: SCR 021713). Tagseq libraries were sequenced using the NovaSeq 6000 SR100 and preprocessed by the Bioinformatics Consulting Group at the University of Texas at Austin. Reads were then processed using the nf-core RNAseq pipeline (28). Briefly, reads were aligned to human reference genome GRCh38 using 'STAR', before quantifying gene counts using 'Salmon' (29, 30).

Differentially expressed genes were determined using edgeR's quasi-likelihood method (31). Differentially expressed genes were defined to have an adjusted p-value < 0.05 (Benjamini-Hotchberg) and log-fold-change of ± 1. Genes, ranked by log-fold-change, were used for gene-set enrichment analysis with fgsea package in R and the Gene Ontology Biological Processes, WikiPathways, KEGG Medicus, and Reactome gene sets (32–37). Significantly enriched pathways were defined as having adjusted p-values < 0.05. To evaluate mixed directional regulations of genes within the pathway Regulation of Mitochondrial Gene Expression we used the subsetting approach described by Väremo et. al.(38) as per instructions. Gene counts and associated code can be found at https://github.com/ZoldanLab/Aging.

# Mitochondrial Analysis:

We assessed mitochondrial membrane potential using tetramethylrhodamine methyl ester (TMRM; Thermo Fisher Scientific). TMRM staining solution was prepared by diluting the 100 µM TMRM stock 1:1000 in EGM2 to a final concentration of 100 nM and immediately used. The cells were then incubated with the TMRM staining solution for 30 min at 37°C. Following incubation, cells were washed 3 times with DPBS and replaced with fresh EGM2. TMRM signal was imaged immediately in live cells using a confocal with a 63x objective (Leica SP8). All images were acquired using identical imaging settings across experimental groups, and fluorescence intensity was quantified from live-cell images using imageJ (39).

We visualized the mitochondrial network 3 days post-differentiation using MitoTracker™ Deep Red FM (Thermo Fisher Scientific; excitation 644 nm) and measured mitochondrial superoxide production with Invitrogen™ MitoSOX™ Green (Thermo Fisher Scientific; excitation 488 nm) Nuclei were stained with Hoechst 33342 (Thermo Fisher Scientific; excitation 350 nm. Stock solutions of MitoSOX™ Green were prepared in anhydrous dimethylformamide (DMF); working solutions were diluted by adding 10 µL of 1 mM stock to 10 mL Hank's Balanced Salt Solution (HBSS). MitoTracker™ Deep Red FM stock was prepared following manufacturer's instructions and diluted in basal EGM2 without supplements. Hoechst

33342 stock was prepared in distilled water; working solutions were diluted by adding 0.1 µL of stock to 10 mL phenol red-free EGM2 without supplement.

Cells were sequentially stained as follows: MitoTracker™ Deep Red FM for 45 min at 37°C, followed by MitoSOX™ Green for 30 min at 37°C, and Hoechst 33342 for 2 min at 37°C, with all steps protected from light. To minimize cell stress during buffer transitions, cells were gently washed with phenol red-free EGM2 basal media after MitoSOX™ staining and before staining with Hoechst 33342. Following staining, cells were washed three times with phenol red-free EGM2 basal media and maintained in the same medium for imaging. All imaging was completed within 2 h of staining completion. At least three regions of interest were imaged with each region having at least three cells visible for a total of 17 cells imaged for ND-hiPSC-EPs and 19 for MD-hiPSC-EPs cells.

Three-dimensional (3D) reconstruction and quantification of nuclei, mitochondria, and mitochondrial superoxide were performed using Imaris software (v10.2.0, Bitplane). Confocal z-stack images acquired in .lif format were converted to Imaris (.ims) files and the “Surface Creation” tool was used to generate 3D surfaces for each subcellular structure using the corresponding fluorescence channel. Nuclei were detected from the Hoechst 33342 channel (excitation 350nm). Machine learning-based segmentation was applied with a surface detail of 0.1µm and slicer extended section of 0.716µm. Nuclear surfaces from dividing cells and cells touching the image boundaries were excluded. Mitochondria were segmented by background subtraction method using the MitoTracker™ Deep Red FM channel (excitation 644 nm). Surface detail was set to 0.075µm and “diameter of the largest sphere which fits into the object” equaled 0.347µm. Local contrast thresholding was performed automatically without manual correction. Surfaces with fewer than 221 voxels were removed. MitoSOX™ Red signal (excitation 488 nm) was used to generate a superoxide surface with surface detail equal to 0.179µm and automatic absolute intensity-based thresholding. To remove non-mitochondrial background signal, a spatial filter was applied whereby MitoSOX™ surfaces with a nearest-neighbor distance > 0.5µm from any mitochondrial surface were excluded from analysis.

## Treatment of hiPSC-EPs With Mitochondrial Specific Antioxidant:

To determine the treatment window required for mitoTEMPO supplementation, MD1-hiPSCs were treated with 1 µM mitoTEMPO (Sigma-Aldrich), a mitochondrial-specific superoxide scavenger, during distinct stages before, during, and after hiPSC-EP differentiation. MD1-hiPSCs were cultured under standard maintenance conditions with or without 1 µM mitoTEMPO for at least three passages prior to differentiation. Cells from both conditions were then differentiated into hiPSC-EPs under standard differentiation conditions or with 1 µM mitoTEMPO supplementation. Following differentiation, $CD34^+$ hiPSC-EPs were isolated by FACS and encapsulated in Collagen/NorHA hydrogels as described above. Encapsulated hiPSC-EPs from all condirions were then cultured for 7 days under standard 3D culture conditions or with 1 µM mitoTEMPO supplementation, resulting in 8 total conditions. Hydrogels were then fixed in 4% PFA, imaged, and computationally analyzed as described above in the network analysis section.

# Statistical Analysis:

Power analysis was performed using independent cell-line means, with each hiPSC line treated as a biological replicate. Using three neonatal donor-derived and three mature donor-derived hiPSC lines, one-sided power was calculated at $\alpha = 0.05$ based on the observed effect sizes.

Unless otherwise stated, comparisons between parameters were done using a one-way ANOVA with individual comparisons between ND-1 and MD-1, ND-2 and MD-2, and ND-3 and MD-3 with * indicating a p-value < 0.05, ** indicating a p-value < 0.001, *** indicating a p-value < 0.0001, and **** indicating a p-value < 0.00001.

## Results

# ND-hiPSCs Yield a Lower Percentage of $CD34^+$ Cells and a Dual $CD31^{+/-}$ Population:

We chose 6 different human induced pluripotent stem cell (hiPSC) lines for use in this study, 3 neonate donor (ND-hiPSC) and 3 mature donor (MD-hiPSC) lines (Fig. 1A). Importantly, each ND-hiPSC line is matched to one MD-hiPSC line by both sex and somatic cell origin (ND-1 with MD-1, ND-2 with MD-2, and ND-3 with MD-3), with the number indicating the corresponding pair. We differentiated all 6 hiPSC lines into endothelial progenitors (hiPSC-EPs) with identical conditions and parameters following our previously described protocol (Fig. 1B) (19). All six hiPSC lines exhibited similar morphological progression throughout differentiation (**S.** Figure 1). By day 5, all six lines expressed the early EP marker CD34, which we used to isolate hiPSC-EPs through FACS.

We used identical gating to sort and quantify $CD34^+$ cells and found that MD-hiPSC lines consistently showed a significantly higher propensity to generate CD34 expressing cells (Fig. 1D). The average $CD34^+$ yield differentiated from MD-hiPSCs was significantly higher in both the matched pairs and higher than any ND-hiPSC line average. Differentiation yields of $CD34^+$ cells for ND-hiPSCs ranged from 8.92–16.49% with a combined average of all replicates of 12.82 ± 5.32%, whereas the yields from all MD-hiPSCs ranged from 18.89–23.81% with an average of 20.68 ± 5.73%.

Although MD-hiPSCs generated a greater fraction of $CD34^+$ cells, all subsequent experiments used equal numbers of sorted $CD34^+$ cells to ensure consistent seeding density. We further characterized the CD34 + cells for CD45 (hematopoietic/immune), CD31 (endothelial), CD140a and CD140b (mural), expression. CD140a expression was significantly lower in MD-hiPSC-EPs than in their matched ND counterparts for donor pairs 1 (0.24-fold, $p < 0.0001$) and 3 (0.25-fold, $p < 0.0001$). In contrast, donor pair 2 exhibited the opposite trend, with significantly higher CD140a expression in MD2 than ND2 (1.53-fold, $p < 0.0001$). No significant differences in CD140b expression were observed between matched ND and MD lines. Across all lines, there were no observed $CD34^+CD45^+$ hematopoietic stem cell populations. Interestingly, within

the sorted $CD34^+$ population, all ND-hiPSC-EP lines exhibited distinct $CD34^+/CD31^+$ and $CD34^+/CD31^-$ populations, whereas MD-hiPSC-EPs were predominantly $CD34^+/CD31^+$. Consistent with this pattern, CD31 expression was significantly higher in MD1 than ND1 (2.24-fold, $p < 0.0001$) and in MD3 than ND3 (1.20-fold, $p = 0.0034$), while higher between MD2 and ND2 the difference was non-significant (1.07-fold) $p = 0.67$ (**S.** Figure 2).

# MD-hiPSC-EPs display diminished vasculogenic potential in 3D hydrogels compared to ND-hiPSC-EPs:

A key feature of hiPSC-EPs is their ability to form lumenized interconnected networks in 3D environments. To evaluate this capacity across the 6 hiPSC-EP lines, we first encapsulated $CD34^+$ hiPSC-EPs in hydrogels composed of an interpenetrating network (IPN) of norbornene-functionalized hyaluronic acid (NorHA) and Collagen I. These hydrogels were formulated at cell densities and stiffness levels previously established by the Zoldan lab as the most optimal for vasculogenesis (7, 19). After encapsulation and seven days of culture in EGM2 supplemented with VEGF, we quantified the resulting cellular structures to determine the vasculogenic potential using a computational pipeline developed by the Zoldan lab (Fig. 2A-F) (11). Interestingly, although the MD-hiPSC lines all showed a higher yield of EPs, (Fig. 1C) the EPs they produced all had reduced vasculogenic potential. Specifically, every ND-hiPSC-EP line developed a similar plexus architecture, whereas all MD-hiPSC-EPs failed to form a lumenized plexus (Fig. 2G).

Unlike the ND-hiPSC-EPs, which generated extensive, lumenized, and highly interconnected vascular structures, the MD-hiPSC-EPs predominantly formed isolated clusters of cells, some with lumens but lacking interconnectivity (Fig. 2D-G). hiPSC-EPs sourced from MD-1 were the only MD-hiPSC-EPs with a similar average vessel diameter as ND-hiPSC-EPs and showed the most lumenized structures, however in all other metrics they underperformed compared to the ND-hiPSC-EPs (Fig. 2A). Between ND-2-hiPSC-EPs and MD-2-hiPSC-EPs (ND-2/MD-2) there is a 58% decrease in average vessel size and between ND-3-hiPSC-EPs and MD-3-hiPSC-EPs (ND-3/MD-3) there is a 45% decrease in average vessel size (Fig. 2A). Other metrics are similarly decreased in structures formed by MD-hiPSC-EPs with the number of end points decreasing by 41% between ND-1-hiPSC-EPs and MD-1-hiPSC-EPs (MD-1/ND-1), 83% (MD-2/ND-2) and 85% (MD-3/ND-3) (Fig. 2B). Cellular structures only occupied 47% (MD-1/ND-1), 16.6% (MD-2/ND-2) and 9.2% (MD-3/ND-3) of the same volume (Fig. 2C). The number of links between vessels decreased by 49% (MD-1/ND-1), 89% (MD-2/ND-2) and 90% (MD-3/ND-3) (Fig. 2D). Interconnectivity was also severely impacted, with less than 10% of MD-hiPSC-EP vessels being connected to the largest vessel, whereas ND-hiPSC-EPs were all between 22.4–22.9% connected (Fig. 2F**)**. This lack of connectivity is further seen with a decrease of 57% (MD-1/ND-1), 93% (MD-2/ND-2), and 95% (MD-3/ND-3) in the number of branch points (Fig. 2E).

**2D Maturation Shows CD31 Emergence in ND-hiPSC-EPs and Altered VE-Cadherin Localization in MD-hiPSC-EPs**:

To investigate potential mechanisms underlying the reduced vasculogenic potential of MD-hiPSC-EPs, we examined the phenotypes of hiPSC-EPs in 2D culture. Although ND-hiPSC-EPs contained a prominent $CD31^-$ population during sorting (**S.** Figure 2), more than 90% of cells across all ND-hiPSC-EPs expressed CD31 after 7 days of culture (**S.** Figure 3) further supporting their endothelial phenotype. Additionally, all ND-hiPSC-EPs formed tight junctions with VE-Cadherin localized to the membrane, consistent with EC identity (**S.** Figure 3A). In contrast, MD-hiPSC-EPs exhibited aberrant VE-cadherin localization, with significantly increased mean perinuclear VE-cadherin signal intensity compared with their matched ND counterparts across all three donor pairs (1.43-fold for MD1 relative to ND1; 1.58-fold for MD2 relative to ND2; 1.58-fold for MD3 relative to ND3; $p < 0.0001$ for all comparisons) (**S.** Figure 3B). Also, despite identical seeding densities, MD-hiPSC-EP cultures showed a statistically significant reduction in cell density compared to ND counterparts. To determine whether this decrease in cell density was due to cellular senescence, we next assessed β-galactosidase (β-gal) expression in 2D culture. Senescence-associated β-gal staining performed at days 3, 5, and 7 of 2D culture did not reveal age-associated differences between ND- and MD-hiPSC-EPs (**S.** Figure 4), and no senescent cells were detected in any cell line at days 3 or 5.

**MD-hiPSC-EPs Display General Hypomethylation with Greater Homogeneity in Methylated CpGs and Greater Heterogeneity in Unmethylated CpGs Compared to ND-hiPSC-EPs**:

We next examined the epigenetic profiles of hiPSC-EPs derived from all six cell lines to determine whether there were consistent differences in DNA methylation patterns that persisted through differentiation. We examined the DNA methylation profiles at over 950,000 CpG sites using the EPICv2 methylation assay from Illumina. Methylation at each CpG site is binary, contributing a beta value (ß) of 1 if methylated and 0 if unmethylated. The average ß value then corresponds with the fraction of cells that are methylated at a specific CpG site in the tested population. Averaging ß values across all sites yields a global methylation level for each sample. Bulk methylation analysis of ß values revealed a clear trend: ND-1-hiPSC-EPs (0.673) and ND-3-hiPSC-EPs (0.657) showed statistically higher global methylation levels across all CpG sites compared to their respective MD counterparts (0.662 & 0.640) (Fig. 3A**&B**). In contrast, ND-2-hiPSC-EPs (0.647) exhibited lower global methylation than MD-2-hiPSC-EP (0.670) However, MDS grouping of hiPSC-EPs placed ND-2 closer to MD-3 than MD-2 and when compared to MD-3-hiPSC-EPs they showed a higher global methylation ß value (0.647 & 0.640) (**S.** Figure 5).

Converting ß-to-M-values, which better capture variability in methylation states (40), we observed further differences in global methylation trends. An M-value of 0 for the CpG probe indicates an equal amount of methylated and unmethylated probe intensity with increasingly positive or negative M-values reflecting either a stronger bias toward methylated or unmethylated signal, respectively. Filtering for only CpG sites with an M-value greater than 0, we found that ND-1-hiPSC-EPs and ND-3-hiPSC-EPs had a greater number of methylated CpG sites (ND-1/MD-1 p-value = 0.045, ND-3/MD-3 p-value = 0.060) and a higher average M value (ND-1/MD-1 p-value = 0.08, ND-3/MD-3 p-value = 0.027) than their matched MD-hiPSC-EP lines (Fig. 3C). When filtered for M values below 0, both ND-1/MD-1 and ND-3/MD-3 comparisons

revealed a statistically significant reduction in the number of CpGs, with ND-1-hiPSC-EPs also showing a significantly lower average M-value (Fig. 3D).

Overall, the global methylation profile was similar between ND-1-hiPSC-EPs, MD-1-hiPSC-EPs and MD-2-hiPSC-EPs, all derived from fibroblasts. Alternatively, ND-2-hiPSC-EPs, ND-3-hiPSC-EPs and MD-3-hiPSC-EPs grouped together, with ND-3 and MD-3 originating from blood-derived cells and ND-2, though reported as fibroblast-derived, aligning more closely with the blood-derived cells' methylation signature.

This grouping observed in global methylation trends was further supported by multidimensional scaling (MDS) analysis of methylation variance between all cell lines (**S.** Figure 5A). Dimension 1, representing the primary eigenvector and accounting for 34% of the total variance, showed strong grouping based on somatic cell origin, excluding ND-2-hiPSC-EPs, which deviated from this pattern and aligned more closely with ND-3-hiPSC-EPs and MD-3-hiPSC-EPs. Dimension 2, explaining 18% of the variance, revealed a weak separation between ND-hiPSC-EPs and MD-hiPSC-EP lines. Additional grouping among ND-hiPSC-EP, but not MD-hiPSC-EP, lines was observed in dimension 5 (11%) (**S.** Figure 5B). No distinct grouping was identified in Dimension 3, which accounted for 15% of the variance. Grouping along higher-variance dimensions indicates that somatic origin is the primary contributor to methylation differences, while separation based on donor age plays a secondary role in variation.

## Differentially Methylated Regions Reveal Donor Age-Associated Differences in Developmental, Mitochondrial, and Vascular Regulatory Pathways:

We further processed the CpG sites by mapping them to the hg38 reference genome and applied the DMRcate algorithm to identify differentially methylated regions (DMRs), which are clusters of CpGs with statistically significant differences in methylation. Each cell line was compared to every other cell line. A consistent trend emerged: comparisons between cell lines of similar somatic cell origin yielded the fewest DMRs. Apart from ND-2/MD-2, all matched ND-MD pairs showed fewer DMRs than unmatched comparisons (**S.** Figure 6A-C). Notably, the ND-2-MD-2 comparison yielded 3,279 DMRs—comparable but less than the ND-2-MD-1 comparison (6959 DMRs) and substantially more than the ND-2-MD-3 comparison (888 DMRs). However, the minimal DMR differences observed in the ND-1/MD-1 and ND-3/MD-3 comparisons support the strategy of using matched pairs to isolate methylation differences attributable to donor age. Given the closer similarity between ND-2-hiPSC-EPs and MD-3-hiPSC-EPs, we included both ND-2-hiPSC-EP/MD-2-hiPSC-EP and ND-2-hiPSC-EP/MD-3-hiPSC-EP (ND-2/MD-3) comparisons in subsequent analyses.

Typically, DMRs are assigned to nearby genes, and their average CpG ß value difference is reported alongside the regions identified. In our analysis, we identified several genes with associated DMRs that were common across all ND-MD comparisons (**S.** Figure 6D). Among these, genes related to the WNT signaling pathway, such as *WNT3A* and *TRRAP*, exhibited less methylation in ND lines compared to MD

lines (41, 42). Notably, *GNAS*, a gene essential for early angiogenesis but not for vasculogenesis, was found to be more methylated in ND lines compared to MD lines (43).

To expand our analysis, we included genes associated with DMRs shared across at least two of the ND-MD matched comparisons, provided the third comparison displayed a methylation difference of less than 10%. This filtering approach identified 266 overlapping DMRs, several of which are associated with genes that are functionally relevant to endothelial cell biology and vasculogenesis (**S. Figure 7A**). Shared trends emerged across these comparisons: ND-1/MD-1 and ND-3/MD-3 showed a consistent increase in methylation in ND lines, whereas ND-2/MD-2, ND-3/MD-3, and ND-2/MD-3 comparisons revealed overlapping sets of genes with decreased methylation in the ND lines (**S. Figure 7A**).

Among the genes displaying shared differential methylation, several are known to play roles in processes critical for vascular development and function. These include *WNT3A*, *FZD-10* and *TRRAP* (WNT signaling) (41, 42, 44), *SPRED-3* (RAS/MAPK signaling) (45), *PLEC*, *CAPZB* and *KIF26B* (cytoskeletal organization and polarity) (46–48), and *CYTH2 (ARNO)*, *ACVRL1*, *GPR75* (vascular development and endothelial signaling) (49–51). In addition, we also found differences in 5 mitochondrial associated genes, *SOD2*, *CAT*, *NDUFA13*, *TXNRD-2* and *PACS2* (52–56), (Fig. 4A).

## MD-hiPSC-EPs Show Greater Predicted Gestational Age:

We assessed the approximate epigenetic age of each line using the Horvath Skin and Blood clock which is a widely used model for predicting chronological age. All lines, except for ND-3 and MD-3, had a negative predicted age (**S. Figure 7C**), with no clear differences observed between cell lines. This suggested that hiPSC-EPs retain fetal signatures similar to hiPSCs, despite progressing through the differentiation process. We therefore applied the Knight epigenetic clock for a more accurate prediction of gestational age. Using this model, ND-1-hiPSC-EPs (5.64 wks) and ND-2-hiPSC-EPs (5.00 wks) were predicted to be significantly younger than MD-1-hiPSC-EPs (8.40 wks) and MD-2-hiPSC-EPs (11.5 wks). ND-3-hiPSC-EPs (7.78 wks) and MD-3-hiPSC-EPs (7.17 wks) showed no statistical difference, although ND-2-hiPSC-EPs showed a significantly younger gestational age prediction than MD-3-hiPSC-EPs (**S. Figure 7D**).

**Transcriptomic Profiling Reveals Strong influence of Somatic Cell Origin and Donor Age-Associated Differences in Mitochondrial Gene Regulation**:

We performed Tagseq RNA sequencing with subsequent normalization and analysis using EdgeR's Trimmed Mean of M-values and quasi-likelihood generalized linear methods. Multidimensional scaling of resulting data was then used to evaluate the global variance between MD- and ND-hiPSC-EPs. From the MDS plot, dimension 1, accounting for 26% inter-sample variance, showed separation of individual donors, with partial clustering of paired donors ND-1–MD-1-hiPSC-EPs and ND-3–MD-3-hiPSC-EPs, and an unexpected grouping of ND-2-hiPSC-EPs with MD-3-hiPSC-EPs, mirroring patterns previously observed in methylation-based clustering (**S. Figure 8A**). Dimension 2 (18% of variance) broadly

separated ND-hiPSC-EP and MD-hiPSC-EP groups, while dimension 4 (9%) showed grouping within the ND-hiPSC-EP samples only (**S. Figure 8B**). No discernible clustering was observed in dimensions 3 (11%) or 5 (7%).

Broad trends showed separation by somatic cell origin using pathway-level analysis of key gene sets, excluding ND-2-hiPSC-EPs, which consistently grouped with ND-3-hiPSC-EPs and MD-3-hiPSC-EPs. Notable exceptions to this trend included specific pathways Regulation of Mitochondrial Gene Expression (Fig. 4B), Nitric Oxide Mediated Signal Transduction (**S. Figure 9A**), Barbed End Actin Filament Capping (**S. Figure 9B**), and Regulation of Extracellular Matrix Organization (**S. Figure 9C**). Among these, Regulation of Mitochondrial Gene Expression was the only pathway that displayed a clear separation between all ND- and MD-hiPSC-EPs, indicating that mitochondrial regulatory processes represent the most pronounced and uniform age-associated transcriptomic difference in these cells.

Within the pathway, examination of overall expression revealed that while ND- and MD-hiPSC-EPs exhibited distinct clustering, there was no uniform directional shift in gene enrichment. Instead, distinct subsets of genes within the pathway showed opposing patterns of expression between the two groups. To capture this mixed directionality, we employed the subsetting approach of Väremo et al.(38), which separates pathway genes into two functionally distinct subsets based on the sign of the t-statistic from a two-sample t-test comparing ND- and MD-hiPSC-EPs. A subset of 22 genes showed significant enrichment in MD-hiPSC-EPs (ssGSEA ES: MD = -0.197 ± 0.061 vs ND = -0.334 ± 0.052, Wilcoxon p = 0.0003). Conversely, a subset of 11 genes showed significant enrichment in ND-hiPSC-EPs (ssGSEA ES: ND = 0.521 ± 0.045 vs MD = 0.400 ± 0.058, Wilcoxon p = 0.0005).

# Mature Donor hiPSC-EPs Exhibit Decreased Mitochondrial Membrane Potential and Elevated Mitochondrial ROS:

The differential regulation by donor age in the pathway Regulation of Mitochondrial Gene Expression, led us to hypothesize that age-associated mitochondrial differences contribute to the differences in vasculogenic potential. This hypothesis was further supported by DNA methylation profiling, which revealed age-dependent differences in the methylation of several mitochondria-associated genes. Notably, genes involved in mitigating mitochondrial ROS, SOD2, CAT, and *TXNRD2* (55–57), remained substantially more methylated in ND-hiPSC-EPs compared to MD hiPSC-EPs (Fig. 4A). Guided by these transcriptomic and epigenetic observations, we next assessed mitochondrial function in a representative ND-hiPSC-EP and MD-hiPSC-EP pair.

We assessed mitochondrial membrane potential using TMRM, a fluorescent dye with increased fluorescence signal in proportion to mitochondrial membrane potential. MD-1-hiPSC-EPs exhibited a 45% reduction in mitochondrial membrane potential compared to ND-1-hiPSC-EPs

(Fig. 4C). Despite a lower membrane potential, we found that MD1-hiPSC-EPs displayed an almost 2-fold (1.8) increase in the median mtROS intensity compared to ND1-hiPSC-EPs (Fig. 4D). In contrast,

morphological mitochondrial metrics, including mitochondrial volume, sphericity, interconnectivity, and disconnected components of the mitochondrial network were unchanged between donors (Fig. 4D), suggesting that the observed mitochondria functionality differences are independent of mitochondria morphology.

# Mitochondrial Specific Antioxidant Pre-treatment Phenotypically Shifts MD1-hiPSC-EPs to a ND-hiPSC-EP State:

To test whether the elevated mtROS contributes to the impaired vasculogenesis, we pre-treated MD1-hiPSCs with mitoTEMPO, a mitochondrial-targeted superoxide scavenger (58), previously shown to reduce mtROS in diabetic adipose derived stem cells (ASCs) and improve the angiogenesis of ASC derived ECs (59) (Fig. 5A). Following three passages of mitoTEMPO treatment, MD1-hiPSCs were differentiated into EPs (MTD1-hiPSC-EPs) and the sorted $CD34^+$ population was characterized for CD45 (hematopoietic), CD31 (endothelial), CD140a and CD140b (mural cell) expression. Within the sorted $CD34^+$ population, MTD1-hiPSC-EPs exhibited a mixed $CD31^+/CD31^-$ population (43% $CD31^+$), comparable to ND1-hiPSC-EPs (36% $CD31^+$) and in marked contrast to untreated MD1-hiPSC-EPs, which were predominantly $CD31^+$ (88%), indicating that mitoTEMPO treatment, shifts MD1 toward the ND1 pattern, restoring the mixed $CD34^+/CD31^+$ and $CD34^+/CD31^-$ progenitor population (Fig. 5B**&C**). CD140a expression was similarly restored in MTD1-hiPSC-EPs (81%) relative to the reduced levels in MD1-hiPSC-EPs (18%), exceeding ND1 levels (56%) while CD140b was elevated in MTD1-hiPSC-EPs (46%) compared to both ND1 (7%) and MD1 (6%). Importantly, CD45 was undetected across all groups, confirming the absence of hematopoietic contamination (Fig. 5B**&C**). Together, these data show that mitoTEMPO treatment restored the CD31-defined immature endothelial progenitor distribution observed in ND1-hiPSC-EPs, while also altering CD140a/CD140b expression within the $CD34^+$ population.

$CD34^+$ MTD-hiPSC-EPs also showed a markedly improved 3D network formation (Fig. 5D). While average vessel diameter remained unchanged, treated MD1-hiPSC-EPs exhibited a 1.8-fold increase in the number of endpoints, a 1.5-fold increase in occupied volume, a 2.0-fold increase in the number of links, a 2.1-fold increase in branch points and a dramatic 3.8 fold increase in the percentage of vessels connected to the largest network compared to untreated MD1-hiPSC-EPs (Fig. 5F). Notably, administering mitoTEMPO only during differentiation or only during 3D network formation did not rescue vasculogenesis (**S. Figure 10**), indicating that sustained reduction of mtROS prior to lineage commitment is required for functional improvement.

# Mitochondrial Specific Antioxidant Pre-treatment Shifts MD1-hiPSC-EPs to a Similar Epigenetic Profile as ND-hiPSC-EPs:

Because mitoTEMPO pretreatment restored vascular plexus formation in MTD1-hiPSC-EPs, we next asked whether this was accompanied by a corresponding shift in the epigenetic landscape. We compared the DNA methylation profiles of ND1-, MD1, and MTD1- hiPSCs and EPs and found that MDS analysis showed MTD1-hiPSC-EPs strongly grouping with ND1-hiPSC-EPs in dimension 2 but not dimension 1 (Fig. 6A).

To determine whether mitoTEMPO treatment restored differentiation-associated CpG changes, we identified CpG sites that changed during hiPSC-to-EP differentiation in each condition and compared their overlap. ND1- and MTD1-hiPSC-EP differentiation shared 29,908 changed CpG sites, including 26,566 CpGs that were also changed in MD1-hiPSC-EPs and 3,342 CpGs that were shared only between ND1 and MTD1. Thus, 11.1% of the CpGs shared between ND1 and MTD1 were not altered in the untreated MD1-hiPSC-EP differentiation, indicating that mitoTEMPO treatment restored a subset of ND-like epigenetic changes that were absent in MD1-hiPSC-EPs. MTD1-hiPSC-EPs also shared 33,562 changed CpGs with MD1-hiPSC-EPs, while retaining 6,996 uniquely changed CpG sites (Fig. 6B).

We next compared the direction and magnitude of methylation changes during differentiation. The number of CpG sites with increased methylation was significantly lower in MD1-hiPSC-EPs than in ND1-hiPSC-EPs, whereas MTD1-hiPSC-EPs showed a number of hypermethylated CpGs comparable to ND1 and significantly greater than MD1. In contrast, the number of CpG sites with decreased methylation remained elevated in both MD1- and MTD1-hiPSC-EPs relative to ND1. The magnitude of methylation gain was highest in ND1-hiPSC-EPs and was reduced in both MD1 and MTD1, while the magnitude of methylation loss did not differ significantly among groups (Fig. 6C).

Finally, to determine whether mitoTEMPO treatment altered transcriptional programs related to chromatin remodeling and epigenetic regulation, we examined differentially expressed genes within the Epigenetic Regulation pathway. Hierarchical clustering of these genes separated ND1-hiPSC-EPs from MD1-hiPSC-EPs, with MTD1-hiPSC-EPs showing alignment with ND1-hiPSC-EPs across a subset of genes (Fig. 6D). Consistent with this shift, pathway enrichment analysis comparing MTD1- and MD1-hiPSC-EPs identified significant enrichment of multiple epigenetic remodeling pathways in MTD1-hiPSC-EPs, including key pathways Regulation of Stem Cell Differentiation, Epigenetic Regulation of Gene Expression and Methylation (**S Fig. 11**). Conversely, MD1-hiPSC-EPs were significantly enriched in pathways suggesting dysfunction and cellular stress, such as the pathways Respiratory Burst, Diseases of Metabolism and Inflammatory Response. Together, these findings indicate that mitoTEMPO pretreatment is associated with coordinated transcriptional remodeling of epigenetic regulatory programs, complementing the observed shift in differentiation-associated DNA methylation toward an ND1-like state.

# Discussion

Many hiPSC lines used in cardiovascular research originate from neonate donors, but future autologous applications will primarily rely on aged donor cells. This disparity warrants further investigation, as prior

studies have shown donor age-associated differences in hiPSCs. With increasing donor age comes an increase in genomic and mitochondrial mutations as well as methylation and gene expression variability (17, 60). While these differences do not appear to impair pluripotency or differentiation capacity, their influence on the functionality of fully differentiated progeny remains understudied (9). To ensure the translational relevance of past research, it is critical to determine whether hiPSC-derived cells from neonatal and aged donors differ in functionality.

Our findings suggest that donor age, must be carefully considered in the development of hiPSC-EP–based vascular therapies. While both ND- and MD-derived hiPSC-EPs undergo EP differentiation (Fig. 1, S. Figure 2&3), MD-derived cells exhibit impaired formation of well-connected, lumenized vascular networks *in vitro* (Fig. 2). These deficits are linked to elevated mtROS in MD-hiPSC-EPs (Fig. 4), which influence epigenetic regulation and developmental priming (Fig. 3–6). Importantly, treatment with a mitochondrial-specific antioxidant effectively restores a ND-hiPSC-EP phenotype (Fig. 6), including *de novo* vascular network formation, demonstrating that the vasculogenic potential of hiPSC-EPs from mature donors can be rescued.

These results extend prior work by Lo Sardo et al., who reported donor age-associated epigenetic differences in hiPSCs from mature donors, but did not include neonatal donors or analyzed differentiated progenitor populations. The elevated mtROS detected in MD-hiPSC-EPs is consistent with reports in the literature suggesting that hiPSCs from older donors harbor mitochondria with accumulated mtDNA mutations (60, 61).

A first indication of intrinsic donor age-dependent differences emerged from consistently higher $CD34^+$ cell yields from differentiated MD-hiPSCs (Fig. 1D), suggesting intrinsic differences in the lineage specification or in expansion capacity. Further phenotypic analysis revealed that all ND-hiPSC lines generated a dual $CD34^+/CD31^-$ and $CD34^+/CD31^+$ population at the time of sorting, whereas MD-hiPSC lines predominantly generated only $CD34^+/CD31^+$ cells (**S.** Figure 2). Because CD31 expression increases with endothelial maturation, the persistence of a $CD34^+/CD31^-$ fraction in ND-hiPSC-EPs suggests that ND-derived cells retain a broader range of endothelial progenitor maturation states at the time of isolation. The absence of CD45 expression in both ND- and MD-hiPSC-EPs at the time of sorting (**S.** Figure 2), combined with robust CD31 expression in more than 85% of both donor groups after 7 days of maturation (**S.** Figure 3), confirms absence of hematopoietic contamination and the endothelial identity of the sorted progenitor populations.

These phenotypic differences were also accompanied by differences in the epigenetic profile. DNA methylation profiling revealed that, ND-hiPSC-EPs consistently exhibited higher average methylated values compared to their matched MD-hiPSC-EP counterparts, with the exception of the ND-2/MD-2 pair (Fig. 3**)**. Given that hypomethylation is associated with both age and hiPSC differentiation (62, 63), the lower methylation levels in the MD lines may reflect underlying disparities in differentiation development, with MD-hiPSC-EPs potentially undergoing accelerated epigenetic remodeling.

Predicted gestational age analysis(26) showed that MD-hiPSC-EPs carry more developmentally advanced epigenetic signatures (**S. Figure 7D**), with greater predicted gestational age in MD-hiPSC confirming our suspicion that MD-hiPSC-EPs undergo accelerated epigenetic progression. Since this window coincides with the developmental shift from vasculogenesis to angiogenesis in early human development (64–66), the more advanced predicted gestational age of MD-hiPSC-EPs may reflect a shift away from the vasculogenic developmental stage and instead toward a more angiogenic state. Gene-level methylation analysis further identified increased methylation at WNT signaling-associated loci in MD-hiPSC-EPs, including genes active during early mesoderm induction (**S. Figure 7A**). These findings suggest that MD-hiPSC-EPs may be epigenetically further removed from early mesodermal and vasculogenic progenitor programs than their ND-hiPSC-EP counterparts.

Importantly, donor-associated methylation differences were not limited to developmental signaling pathways. We also observed donor age-associated methylation differences of genes involved in mitochondrial regulation and mitochondrial ROS homoeostasis, including SOD2, CAT, TXNRD2, NDUFA13, and PACS2 (Fig. 4A). Based on the decrease of methylation in MD-hiPSC-EPs of SOD2 and CAT this suggested activation of antioxidant defense mechanisms in MD-hiPSC-EPs.

These differences prompted us to consider mitochondrial functionality in MD-hiPSC-EPs. Given that hiPSCs primarily rely on glycolysis during early stages, such differences might not be readily apparent before differentiation (67). Direct functional assessment confirmed that MD1-hiPSC-EPs exhibited significantly lower mitochondrial membrane potential and significantly higher mtROS than ND1-hiPSC-EPs (Fig. 5C**&D**). This increase is consistent with prior literature (68), and with our findings of the increased methylation of mtROS associated genes (Fig. 4A). Epigenetic analysis further supports the presence of elevated mtROS, as oxidative stress is known to drive both locus-specific demethylation, such as at *TBX5* (69), where MD1-hiPSC-EPs showed a substantial average 0.6 decrease in ß-value and broader global hypomethylation, observed in MD-hiPSC-EPs (Fig. 3).

Critically, sustained culture of MD1-hiPSCs with the mitochondrial-specific antioxidant mitoTEMPO significantly improved the vasculogenic capacity of MD1-hiPSC-EPs, restoring network formation toward the level observed in ND-hiPSC-EPs (Fig. 2, Fig. 5). This rescue was dependent on treatment timing, as vasculogenic potential was restored only when mitoTEMPO was administered before EP differentiation (**S. Figure 15**). These results identify the hiPSC stage as the critical window during which donor age-associated mitochondrial dysfunction exerts its effects, although the resulting mitochondrial and functional deficits become most apparent after endothelial differentiation. Importantly, mitoTEMPO treatment shifted the phenotypic, epigenetic and transcriptional profile of MD1-hiPSC-EPs towards the ND1-hiPSC-EP phenotype (Fig. 5, Fig. 6). Phenotypically, mitoTEMPO treatment restored the mixed $CD34^{+}/CD31^{-}$ and $CD34^{+}/CD31^{+}$ population observed in ND-hiPSC-EPs. At the epigenetic level, MTD1-hiPSC-EPs shared a substantial subset of differentiation-associated CpG changes with ND1-hiPSC-EPs that were not observed in untreated MD1-hiPSC-EPs (Fig. 6A-C). Transcriptionally, MD-hiPSC-EPs grouped with ND-hiPSC-EPs in a subset of the pathway, Epigenetic Regulation (Fig. 6D). Thus,

mitoTEMPO did not simply improve vascular network formation, but redirected the MD1-hiPSC-EP differentiation trajectory toward an ND-like state.

Although we were able to rescue the MD phenotype in our hiPSC-EP based model, other groups have generated lumenized vascular networks using MD-hiPSC-derived ECs, rather than EPs, by providing substantial exogenous support (68), including co-culture with mural cells, low matrix stiffness, pulsatile flow, and high cell density (70). Importantly, in the absence of these cues, little to no network formation was observed. While these findings highlight the context-dependent capacity of mature ECs to form vascular networks, additional studies are needed to determine whether our observations translate to systems utilizing mature ECs and perfused microfluidic platforms, where factors such as flow and vessel maturation may further influence cellular behavior. Future work should also focus on identifying the exact mechanisms responsible for reduced mitochondrial function in MD-hiPSC-EPs and determining how supportive cues, such as targeted growth factor supplementation or *in vivo* paracrine interactions, influence vasculogenesis. A limitation of this study is the relatively small cohort size of three ND and three MD donor-derived hiPSC lines, due to the substantial characterization required for each independent line. However, donor-derived lines, rather than technical replicates, were used as the biological units for statistical analysis, and the major ND-versus-MD functional differences were directionally consistent across lines. Larger cohorts with targeted studies will be needed to fully define donor-to-donor variability. Together, these findings underscore the influence of donor background on hiPSC-EP function, identify mitochondrial dysfunction as a contributor to donor age-associated vasculogenic impairment, and suggest mitochondrial antioxidant treatment as a potential strategy for functional rescue.

## Declarations

# Sources of Funding:

We gratefully acknowledge the support from the National Institute of Health (F31HL176136) awarded to Bryce Larsen and the partial support from the National Institutes of Health (R01HL15829) and the Harry S. Moss Heart Trust (UTAUS-FA00002510), both awarded to Janet Zoldan.

# Disclosures:

None.

# Author Contribution

B.L. wrote and edited the manuscript text, collected data, prepared figures and supplied funding. C.C. collected data and wrote some sections of the manuscript. A.R. collected and processed data. A.M.

collected and processed data. W.W. collected and processed data. S.F. collected and processed data. J.Z. wrote and edited the manuscript and supplied funding.


# Acknowledgement

We would like to thank Dr. Adrianne Rosales and Katie Halwachs for their support with the NorHA Collagen hydrogel material formulation as well as Brett Stern for optimizing the hiPSC-EP differentiation method.


# Data Availability

Data Availability Statement: Multi-omics data including raw gene counts and .idat files as well as R scripts underlying this article are available at https://github.com/ZoldanLab/Aging. All other data will be shared on reasonable request to the corresponding author.

## References


1. Celermajer DS, Chow CK, Marijon E, Anstey NM, Woo KS. Cardiovascular disease in the developing world: Prevalences, patterns, and the potential of early disease detection. J Am Coll Cardiol. 2012;60(14):1207–16. doi:10.1016/j.jacc.2012.03.074 PubMed PMID: 22858388.
2. Tsao CW, Aday AW, Almarzooq ZI, Anderson CAM, Arora P, Avery CL, et al. Heart Disease and Stroke Statistics – 2023 Update: A Report from the American Heart Association. Circulation. 2023. 93–621 p. doi:
10.
1161/CIR.0000000000001123 PubMed PMID: 36695182.
3. Sniderman AD, Furberg CD. Age as a modifiable risk factor for cardiovascular disease. The Lancet. 2008;371(9623):1547–9. doi:10.1016/S0140-6736(08)60313-X PubMed PMID: 18321568.
4. Ungvari Z, Tarantini S, Donato AJ, Galvan V, Csiszar A. Mechanisms of vascular aging. Circ Res. 2018;123(7):849–67. doi:10.1161/CIRCRESAHA.118.311378 PubMed PMID: 30355080.
5. Wiegand C, Banerjee I. Recent advances in the applications of iPSC technology. Curr Opin Biotechnol. 2019;60:250–8. doi:10.1016/j.copbio.2019.05.011 PubMed PMID: 31386977.
6. Takahashi K, Yamanaka S. Induction of Pluripotent Stem Cells from Mouse Embryonic and Adult Fibroblast Cultures by Defined Factors. Cell. 2006;126(4):663–76. doi:10.1016/j.cell.2006.07.024 PubMed PMID: 16904174.
7. Crosby CO, Hillsley A, Kumar S, Stern B, Parekh SH, Rosales A, et al. Phototunable interpenetrating polymer network hydrogels to stimulate the vasculogenesis of stem cell-derived endothelial progenitors. Acta Biomater. 2021;122:133–44. doi:10.1016/j.actbio.2020.12.041 PubMed PMID: 33359297.

8. Hu S, Zhao MT, Jahanbani F, Shao NY, Lee WH, Chen H, et al. Effects of cellular origin on differentiation of human induced pluripotent stem cell-derived endothelial cells. Journal of Clinical Investigation. 2016;1(8):1–12. doi:10.1172/jci.insight.85558 PubMed PMID: 27398408.
9. Kränkel N. Age Is Relative — Impact of Donor Age on Induced Pluripotent Stem Cell-Derived Cell Functionality. Vol. 5. 2018;5(January):1–8. doi:10.3389/fcvm.2018.00004
10. Schnellmann R, Ntekoumes D, Choudhury MI, Sun S, Wei Z, Gerecht S. Stiffening Matrix Induces Age-Mediated Microvascular Phenotype Through Increased Cell Contractility and Destabilization of Adherens Junctions. Advanced Science. 2022;9(22):1–13. doi:10.1002/advs.202201483 PubMed PMID: 35657074.
11. Crosby CO, Valliappan D, Shu D, Kumar S, Tu C, Deng W, et al. Quantifying the Vasculogenic Potential of Induced Pluripotent Stem Cell-Derived Endothelial Progenitors in Collagen Hydrogels. Tissue Eng Part A. 2019;25(9–10):746–58. doi:10.1089/ten.tea.2018.0274 PubMed PMID: 30618333.
12. Xu B, Shimauchi-Ohtaki H, Yoshimoto Y, Sadakata T, Ishizaki Y. Transplanted human iPSC-derived vascular endothelial cells promote functional recovery by recruitment of regulatory T cells to ischemic white matter in the brain. J Neuroinflammation. 2023;20(1):1–13. doi:10.1186/s12974-023-02694-0 PubMed PMID: 36650518.
13. Atchison L, Abutaleb NO, Snyder-Mounts E, Gete Y, Ladha A, Ribar T, et al. iPSC-Derived Endothelial Cells Affect Vascular Function in a Tissue-Engineered Blood Vessel Model of Hutchinson-Gilford Progeria Syndrome. Stem Cell Reports. 2020;14(2):325–37. doi:10.1016/j.stemcr.2020.01.005 PubMed PMID: 32032552.
14. Lian X, Bao X, Al-Ahmad A, Liu J, Wu Y, Dong W, et al. Efficient differentiation of human pluripotent stem cells to endothelial progenitors via small-molecule activation of WNT signaling. Stem Cell Reports. 2014;3(5):804–16. doi:10.1016/j.stemcr.2014.09.005 PubMed PMID: 25418725.
15. Katt ME, Xu ZS, Gerecht S, Searson PC. Human brain microvascular endothelial cells derived from the BC1 iPS cell line exhibit a blood-brain barrier phenotype. PLoS One. 2016;11(4):1–18. doi:10.1371/journal.pone.0152105 PubMed PMID: 27070801.
16. Martin SS, Aday AW, Allen NB, Almarzooq ZI, Anderson CAM, Arora P, et al. 2025 Heart Disease and Stroke Statistics: A Report of US and Global Data From the American Heart Association. Circulation. 2025;151(8). doi:10.1161/CIR.0000000000001303
17. Lo Sardo V, Ferguson W, Erikson GA, Topol EJ, Baldwin KK, Torkamani A. Influence of donor age on induced pluripotent stem cells. Nat Biotechnol. 2017;35(1):69–74. doi:10.1038/nbt.3749 PubMed PMID: 27941802.
18. Stern B, Monteleone P, Zoldan J. SARS-CoV-2 spike protein induces endothelial dysfunction in 3D engineered vascular networks. J Biomed Mater Res A. 2024;112(4):524–33. doi:10.1002/jbm.a.37543 PubMed PMID: 37029655.
19. Stern BMSLBBAZJ. Differentiation Protocol-Dependent Variability in hiPSC-Derived Endothelial Progenitor Functionality. Regen Eng Transl Med. 2025 Apr 3.

20. Jalilian E, Raimes W. Transcriptional profiling reveals fundamental differences in iPS-derived progenitors of endothelial cells (PECs) versus adult circulating EPCs. 1–24.
21. Wagner V, Gil J. Senescence as a therapeutically relevant response to CDK4/6 inhibitors. Oncogene. Springer Nature; 2020. p. 5165–76. doi:10.1038/s41388-020-1354-9 PubMed PMID: 32541838.
22. Peters TJ, Meyer B, Ryan L, Achinger-Kawecka J, Song J, Campbell EM, et al. Characterisation and reproducibility of the HumanMethylationEPIC v2.0 BeadChip for DNA methylation profiling. BMC Genomics. 2024;25(1). doi:10.1186/s12864-024-10027-5 PubMed PMID: 38448820.
23. Zhou W, Triche TJ, Laird PW, Shen H. SeSAMe: Reducing artifactual detection of DNA methylation by Infinium BeadChips in genomic deletions. Nucleic Acids Res. 2018;46(20):1–15. doi:10.1093/nar/gky691 PubMed PMID: 30085201.
24. Horvath S, Oshima J, Martin GM, Lu AT, Quach A, Cohen H, et al. Epigenetic clock for skin and blood cells applied to Hutchinson Gilford Progeria Syndrome and ex vivo studies. AGING [Internet]. 2018. Available from: www.aging-us.com
25. Pelegi-Siso D, De Prado P, Ronkainen J, Bustamante M, Gonzalez JR. Methylclock: A Bioconductor package to estimate DNA methylation age methylclock: A Bioconductor package to estimate DNA methylation age. Bioinformatics. 2021;37(12):1759–60. doi:10.1093/bioinformatics/btaa825 PubMed PMID: 32960939.
26. Knight AK, Craig JM, Theda C, Bækvad-Hansen M, Bybjerg-Grauholm J, Hansen CS, et al. An epigenetic clock for gestational age at birth based on blood methylation data. Genome Biol. 2016;17(1). doi:10.1186/s13059-016-1068-z PubMed PMID: 27717399.
27. Peters TJ, Buckley MJ, Chen Y, Smyth GK, Goodnow CC, Clark SJ. Calling differentially methylated regions from whole genome bisulphite sequencing with DMRcate. Nucleic Acids Res. 2021;49(19). doi:10.1093/nar/gkab637 PubMed PMID: 34320181.
28. Ewels PA, Peltzer A, Fillinger S, Patel H, Alneberg J, Wilm A, et al. The nf-core framework for community-curated bioinformatics pipelines. Nature Biotechnology. Nature Research; 2020. p. 276–8. doi:10.1038/s41587-020-0439-x PubMed PMID: 32055031.
29. Dobin A, Davis CA, Schlesinger F, Drenkow J, Zaleski C, Jha S, et al. STAR: Ultrafast universal RNA-seq aligner. Bioinformatics. 2013;29(1):15–21. doi:10.1093/bioinformatics/bts635 PubMed PMID: 23104886.
30. Patro R, Duggal G, Love MI, Irizarry RA, Kingsford C. Salmon provides fast and bias-aware quantification of transcript expression. Nat Methods. 2017;14(4):417–9. doi:10.1038/nmeth.4197 PubMed PMID: 28263959.
31. Chen Y, Chen L, Lun ATL, Baldoni PL, Smyth GK. edgeR v4: powerful differential analysis of sequencing data with expanded functionality and improved support for small counts and larger datasets. Nucleic Acids Res. 2025;53(2). doi:10.1093/nar/gkaf018
32. Aleksander SA, Balhoff J, Carbon S, Cherry JM, Drabkin HJ, Ebert D, et al. The Gene Ontology knowledgebase in 2023. Genetics. 2023;224(1). doi:10.1093/genetics/iyad031 PubMed PMID: 36866529.

33. Ashburner M, Ball CA, Blake JA, Botstein D, Butler H, Cherry JM, et al. Gene Ontology: tool for the unification of biology The Gene Ontology Consortium* [Internet]. 2000. Available from: http://www.flybase.bio.indiana.edu
34. Pico AR, Kelder T, Van Iersel MP, Hanspers K, Conklin BR, Evelo C. WikiPathways: Pathway Editing for the People. PLoS Biology. 2008. p. 1403–7. doi:10.1371/journal.pbio.0060184 PubMed PMID: 18651794.
35. Kanehisa M, Goto S. KEGG: Kyoto Encyclopedia of Genes and Genomes. Nucleic Acids Research [Internet]. 2000. Available from: http://www.genome.ad.jp/kegg/
36. Kanehisa M, Furumichi M, Sato Y, Matsuura Y, Ishiguro-Watanabe M. KEGG: biological systems database as a model of the real world. Nucleic Acids Res. 2025;53(D1):D672–7. doi:10.1093/nar/gkae909 PubMed PMID: 39417505.
37. Milacic M, Beavers D, Conley P, Gong C, Gillespie M, Griss J, et al. The Reactome Pathway Knowledgebase 2024. Nucleic Acids Res. 2024;52(D1):D672–8. doi:10.1093/nar/gkad1025 PubMed PMID: 37941124.
38. Väremo L, Nielsen J, Nookaew I. Enriching the gene set analysis of genome-wide data by incorporating directionality of gene expression and combining statistical hypotheses and methods. Nucleic Acids Res. 2013;41(8):4378–91. doi:10.1093/nar/gkt111 PubMed PMID: 23444143.
39. Haznadar M. Cancer Metabolism Methods and Protocols Methods in Molecular Biology 1928 [Internet]. Available from: http://www.springer.com/series/7651
40. Du P, Zhang X, Huang CC, Jafari N, Kibbe WA, Hou L, et al. Comparison of Beta-value and M-value methods for quantifying methylation levels by microarray analysis. BMC Bioinformatics. 2010;11(1):587. doi:10.1186/1471-2105-11-587 PubMed PMID: 21118553.
41. Tran TH, Wang X, Browne C, Zhang Y, Schinke M, Izumo S, et al. Wnt3a-induced mesoderm formation and cardiomyogenesis in human embryonic stem cells. Stem Cells. 2009;27(8):1869–78. doi:10.1002/stem.95 PubMed PMID: 19544447.
42. Finkbeiner MG, Sawan C, Ouzounova M, Murr R, Herceg Z. HAT cofactor TRRAP mediates β-catenin ubiquitination on the chromatin and the regulation of the canonical Wnt pathway. Cell Cycle. 2008;7(24):3908–14. doi:10.4161/cc.7.24.7354 PubMed PMID: 19066453.
43. Shao X, Liu K, Fan Y, Ding Z, Chen M, Zhu M, et al. Gαs Relays Sphingosine-1-Phosphate Receptor 1 Signaling to Stabilize Vascular Endothelial-Cadherin at Endothelial Junctions to Control Mouse Embryonic Vascular Integrity. Journal of Genetics and Genomics. 2015;42(11):613–24. doi:10.1016/j.jgg.2015.08.006 PubMed PMID: 26674379.
44. Terasaki H, Saitoh T, Shiokawa K, Katoh M. Frizzled-10, up-regulated in primary colorectal cancer, is a positive regulator of the WNT-B-catenin-TCF signaling pathway. INTERNATIONAL JOURNAL OF MOLECULAR MEDICINE. 2002.
45. Nonami A, Kato R, Taniguchi K, Yoshiga D, Taketomi T, Fukuyama S, et al. Spred-1 negatively regulates interleukin-3-mediated ERK/mitogen-activated protein (MAP) kinase activation in

hematopoietic cells. Journal of Biological Chemistry. 2004;279(50):52543–51. doi: 10.1074
/jbc.M405189200 PubMed PMID: 15465815.

46. Wiche G, Winter L. Plectin isoforms as organizers of intermediate filament cytoarchitecture. Bioarchitecture. 2011;1(1):14–20. doi:10.4161/bioa.1.1.14630
47. Cooper JA, Sept D. New Insights into Mechanism and Regulation of Actin Capping Protein. International Review of Cell and Molecular Biology. 2008. p. 183–206. doi:10.1016/S1937-6448(08)00604-7 PubMed PMID: 18544499.
48. Guillabert-Gourgues A, Jaspard-Vinassa B, Bats ML, Sewduth RN, Franzl N, Peghaire C, et al. Kif26b controls endothelial cell polarity through the Dishevelled/Daam1-dependent planar cell polaritysignaling pathway. Mol Biol Cell. 2016;27(6):941–53. doi:10.1091/mbc.E14-08-1332 PubMed PMID: 26792835.
49. Mannell HK, Pircher J, Chaudhry DI, Alig SKC, Koch EG, Mettler R, et al. ARNO regulates VEGF-dependent tissue responses by stabilizing endothelial VEGFR-2 surface expression. Cardiovasc Res. 2012;93(1):111–9. doi:10.1093/cvr/cvr265 PubMed PMID: 22002459.
50. Fan F, Roman RJ. GPR75 Identified as the First 20-HETE Receptor: A Chemokine Receptor Adopted by a New Family. Circulation Research. Lippincott Williams and Wilkins; 2017. p. 1696–8. doi:10.1161/CIRCRESAHA.117.311022 PubMed PMID: 28546348.
51. Wang G, Wen B, Deng Z, Zhang Y, Kolesnichenko OA, Ustiyan V, et al. Endothelial progenitor cells stimulate neonatal lung angiogenesis through FOXF1-mediated activation of BMP9/ACVRL1 signaling. Nat Commun. 2022;13(1). doi:10.1038/s41467-022-29746-y PubMed PMID: 35440116.
52. Hu H, Nan J, Sun Y, Zhu D, Xiao C, Wang Y, et al. Electron leak from NDUFA13 within mitochondrial complex I attenuates ischemia-reperfusion injury via dimerized STAT3. Proc Natl Acad Sci U S A. 2017;114(45):11908–13. doi:10.1073/pnas.1704723114 PubMed PMID: 29078279.
53. Yoshioka J. Thioredoxin Reductase 2 (Txnrd2) Regulates Mitochondrial Integrity in the Progression of Age-Related Heart Failure. Journal of the American Heart Association. 2015. doi:10.1161/JAHA.115.002278 PubMed PMID: 26199229.
54. Li C, Li L, Yang M, Zeng L, Sun L. PACS-2: A key regulator of mitochondria-associated membranes (MAMs). Pharmacological Research. Academic Press; 2020. doi:10.1016/j.phrs.2020.105080 PubMed PMID: 32673704.
55. Panieri E, Santoro MM. ROS signaling and redox biology in endothelial cells. Cellular and Molecular Life Sciences. 2015;72(17):3281–303. doi:10.1007/s00018-015-1928-9 PubMed PMID: 25972278.
56. He J, Liu X, Su C, Wu F, Sun J, Zhang J, et al. Inhibition of Mitochondrial Oxidative Damage Improves Reendothelialization Capacity of Endothelial Progenitor Cells via SIRT3 (Sirtuin 3)-Enhanced SOD2 (Superoxide Dismutase 2) Deacetylation in Hypertension. Arterioscler Thromb Vasc Biol. 2019;39(8):1682–98. doi:
10.1161
/ATVBAHA.119.312613 PubMed PMID: 31189433.

57. Yoshioka J. Thioredoxin Reductase 2 (Txnrd2) Regulates Mitochondrial Integrity in the Progression of Age-Related Heart Failure. Journal of the American Heart Association. 2015. doi:10.1161/JAHA.115.002278 PubMed PMID: 26199229.

58. Dikalova AE, Bikineyeva AT, Budzyn K, Nazarewicz RR, McCann L, Lewis W, et al. Therapeutic targeting of mitochondrial superoxide in hypertension. Circ Res. 2010;107(1):106–16. doi:10.1161/CIRCRESAHA.109.214601 PubMed PMID: 20448215.

59. Lian K, Wang Q, Zhao S, Yang M, Chen G, Chen Y, et al. Pretreatment of Diabetic Adipose-derived Stem Cells with mitoTEMPO Reverses their Defective Proangiogenic Function in Diabetic Mice with Critical Limb Ischemia. Cell Transplant. 2019;28(12):1652–63. doi:10.1177/0963689719885076 PubMed PMID: 31684763.

60. Carelli V, Hirano M, Enríquez JA, Chinnery PF. Implications of mitochondrial DNA mutations in human induced pluripotent stem cells. Nat Rev Genet. 2022;23(2):69–70. doi:10.1038/s41576-021-00430-z PubMed PMID: 34728812.

61. Prigione A, Bjo¨ B, Lichtner B, Kuhl H, Struys EA, Wamelink M, et al. EMBRYONIC STEM CELLS/INDUCED PLURIPOTENT STEM CELLS Human Induced Pluripotent Stem Cells Harbor Homoplasmic and Heteroplasmic Mitochondrial DNA Mutations While Maintaining Human Embryonic Stem Cell-like Metabolic Reprogramming. Stem Cells. 2011;29:1338–48. doi:10.1002/stem

62. Ankam S, Rovini A, Baheti S, Hrstka R, Wu Y, Schmidt K, et al. DNA methylation patterns in human iPSC-derived sensory neuronal differentiation. Epigenetics. 2019;14(9):927–37. doi:10.1080/15592294.2019.1625672 PubMed PMID: 31148524.

63. Tollefsbol TO. Epigenetics of aging. Epigenetics of Aging. Springer New York; 2010. 1–469 p. doi:10.1007/978-1-4419-0639-7

64. Czirok A, Little CD. Pattern formation during vasculogenesis. Birth Defects Research Part C - Embryo Today: Reviews. 2012. p. 153–62. doi:10.1002/bdrc.21010 PubMed PMID: 22692888.

65. Risau W. Mechanisms of angiogenesis.

66. Schmidt A, Brixius K, Bloch W. Endothelial precursor cell migration during vasculogenesis. Circulation Research. 2007. p. 125–36. doi:10.1161/CIRCRESAHA.107.148932 PubMed PMID: 17641236.

67. Varum S, Rodrigues AS, Moura MB, Momcilovic O, Easley IV CA, Ramalho-Santos J, et al. Energy metabolism in human pluripotent stem cells and their differentiated counterparts. PLoS One. 2011;6(6). doi:10.1371/journal.pone.0020914 PubMed PMID: 21698063.

68. Kang E, Wang X, Tippner-Hedges R, Ma H, Folmes CDL, Gutierrez NM, et al. Age-related accumulation of somatic mitochondrial DNA mutations in adult-derived human ipscs. Cell Stem Cell. 2016;18(5):625–36. doi:10.1016/j.stem.2016.02.005 PubMed PMID: 27151456.

69. Agnes Görlach C, Kietzmann T, Petry A, Shvetsova A, Gerhold JM, Görlach A. Themed Section: Redox Biology and Oxidative Stress in Health and Disease. Br J Pharmacol. 2017;174:1533. doi:10.1111/bph.v174.12/issuetoc

70. Bulut M, Vila Cuenca M, de Graaf M, van den Hil FE, Mummery CL, Orlova V V. Three-Dimensional Vessels-on-a-Chip Based on hiPSC-derived Vascular Endothelial and Smooth Muscle Cells. Curr Protoc. 2022;2(10). doi:10.1002/cpz1.564 PubMed PMID: 36250774.

# Figures

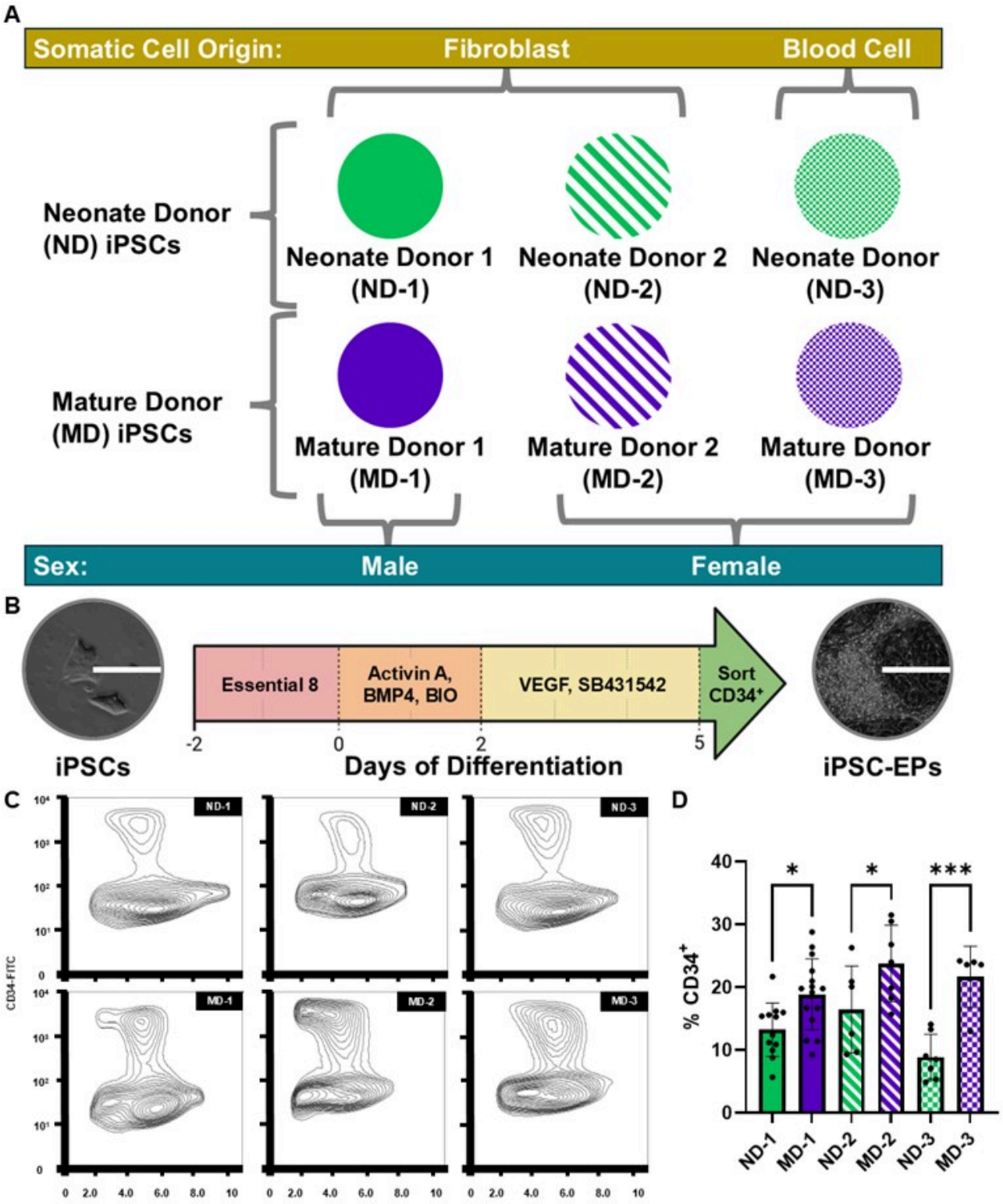



**Figure 1**

(A) Schematic illustrating the donor age, somatic cell source, and sex of the six iPSC lines used in this study. Colors and patterns assigned to each cell line are consistent across all figures. (B) Overview of iPSC differentiation to EPs . Representative bright field images of iPSCs colonies before mesoderm induction (left) and cells shortly before flow sorting (right). Scale bar: 200 μm. Figure 2. (C) Representative contour plots showing $CD34^+$ and $CD34^-$ populations from Day 5 differentiated iPSCs stained with anti-CD34. (D) Quantification of $CD34^+$ cell yields across all six iPSC lines. MD-iPSC lines consistently produce a higher percentage of $CD34^+$ cells compared to their matched ND-iPSC counterparts, as well as relative to all other ND-iPSC lines. One-way ANOVA with pairwise comparisons between ND-1/MD-1, ND-2/MD-2, and ND-3/MD-3. *$p < 0.05$, ***$p < 0.0001$. N = 5–15 independent differentiations.

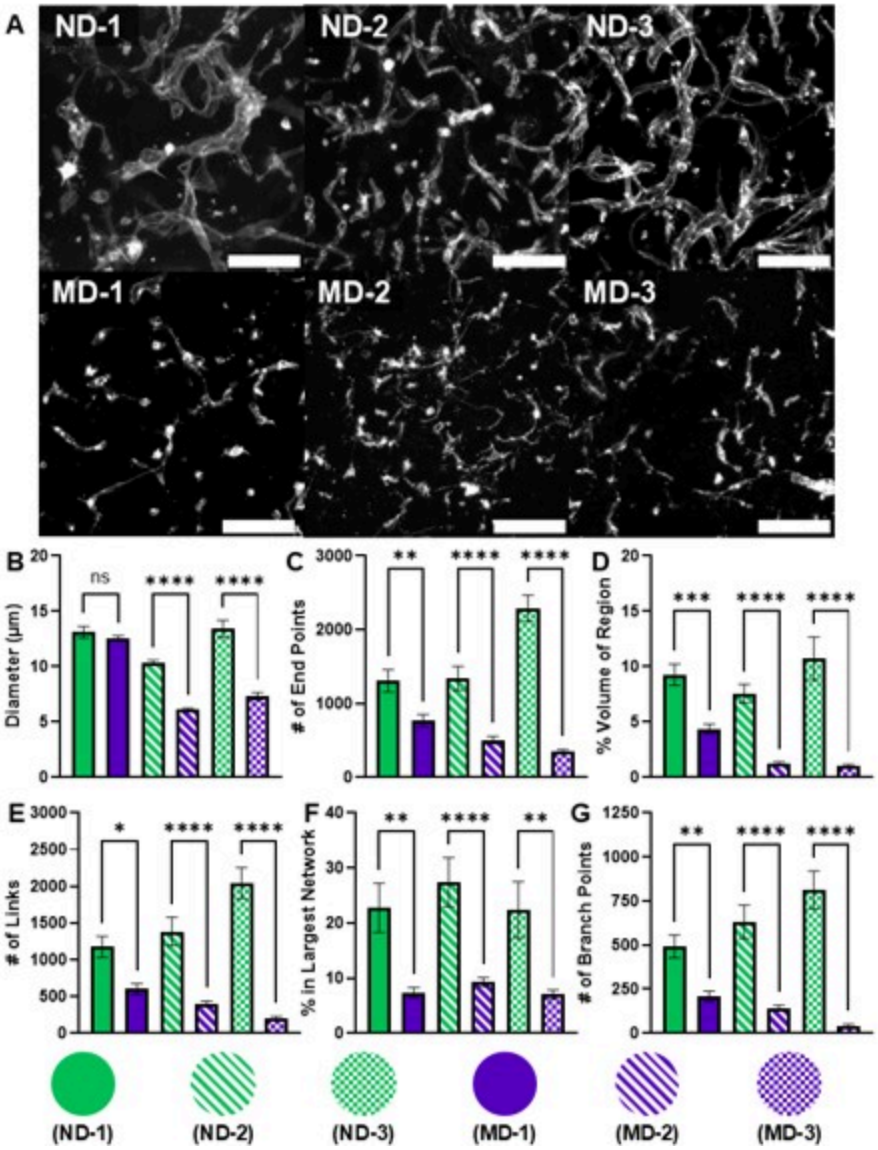



**Figure 2**

(A) Representative 50-100 μm deep Z-stack projection of the resulting micro vessel formed after encapsulating iPSC-EPs, differentiated from the six cell lines, in hydrogels and culturing for 7 days.

Interconnected lumenized structures are observed in each ND-iPSC-EP line, while such structures are largely absent in the MD-iPSC-EP lines. (B) Average diameter of micro vessels (μm). (C) Average number of end points. These differences are reflected in the quantified vascular network metrics: (D) Total volume that is occupied by micro vessels (%). (E) The number of links between micro vessels. (F) The percent of micro vessels that are connected to the largest micro vessel. (G) The number of branch points within micro vessels. N = 11-18 regions of interest from at least 3 independent differentiations. One-way-ANOVA with comparisons between ND-1/MD-1, ND-2/MD-2 and ND-3/MD-3. * = p<0.05, ** = p<0.01, *** = p<0.0001, **** = p<0.00001. Scale bar: 200 μm.

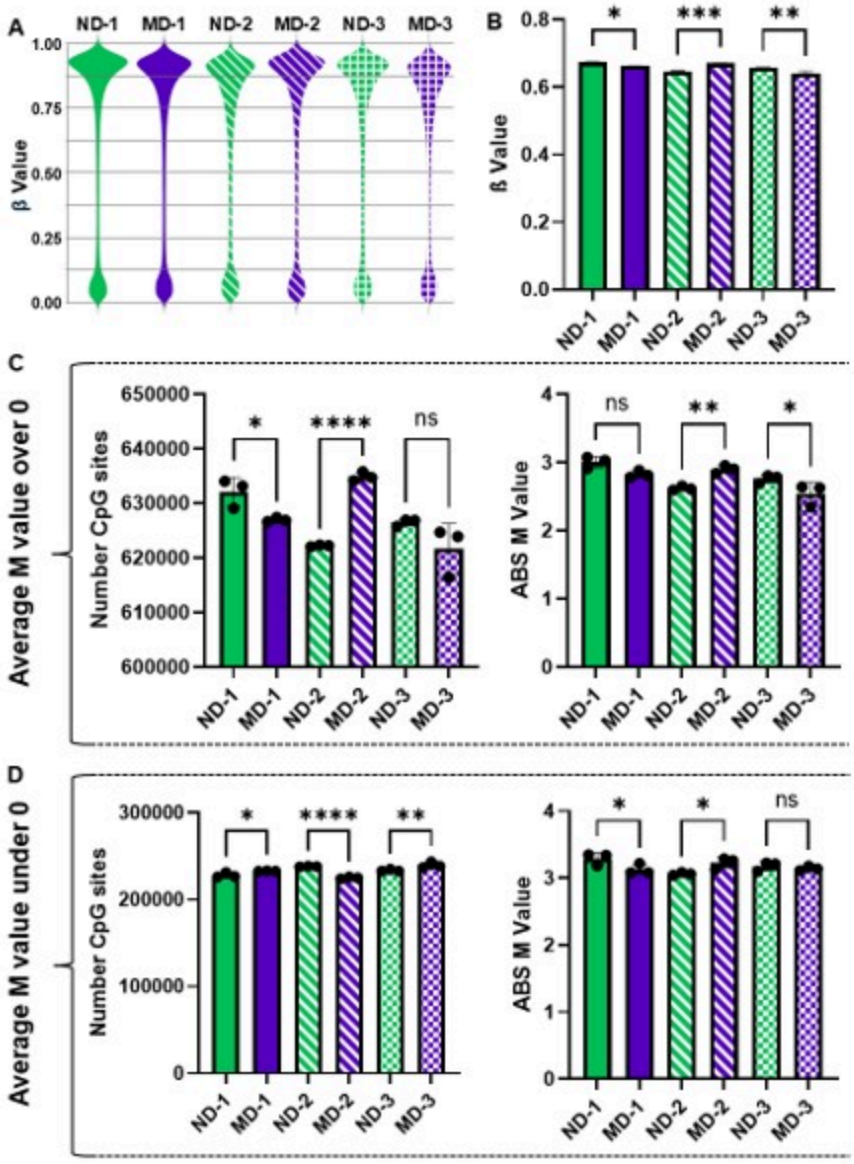



**Figure 3**

(A) Violin plots of beta values showing global methylation trends across all CpG sites, with ND1 and ND3 exhibiting higher overall methylation than their MD counterparts. (B) Total average ß methylation value for all CpG sites. (C) Total number of CpG sites and average M value for all CpG sites with an M value over 0. (D) Total number of CpG sites and average M value for all CpG sites with an M value below 0. N =

3 independent differentiations. One-way-ANOVA with comparisons between ND-1/MD-1, ND-2/MD-2 and ND-3/MD-3. * = p<0.05, ** = p<0.01, *** = p<0.0001, **** = p<0.00001.

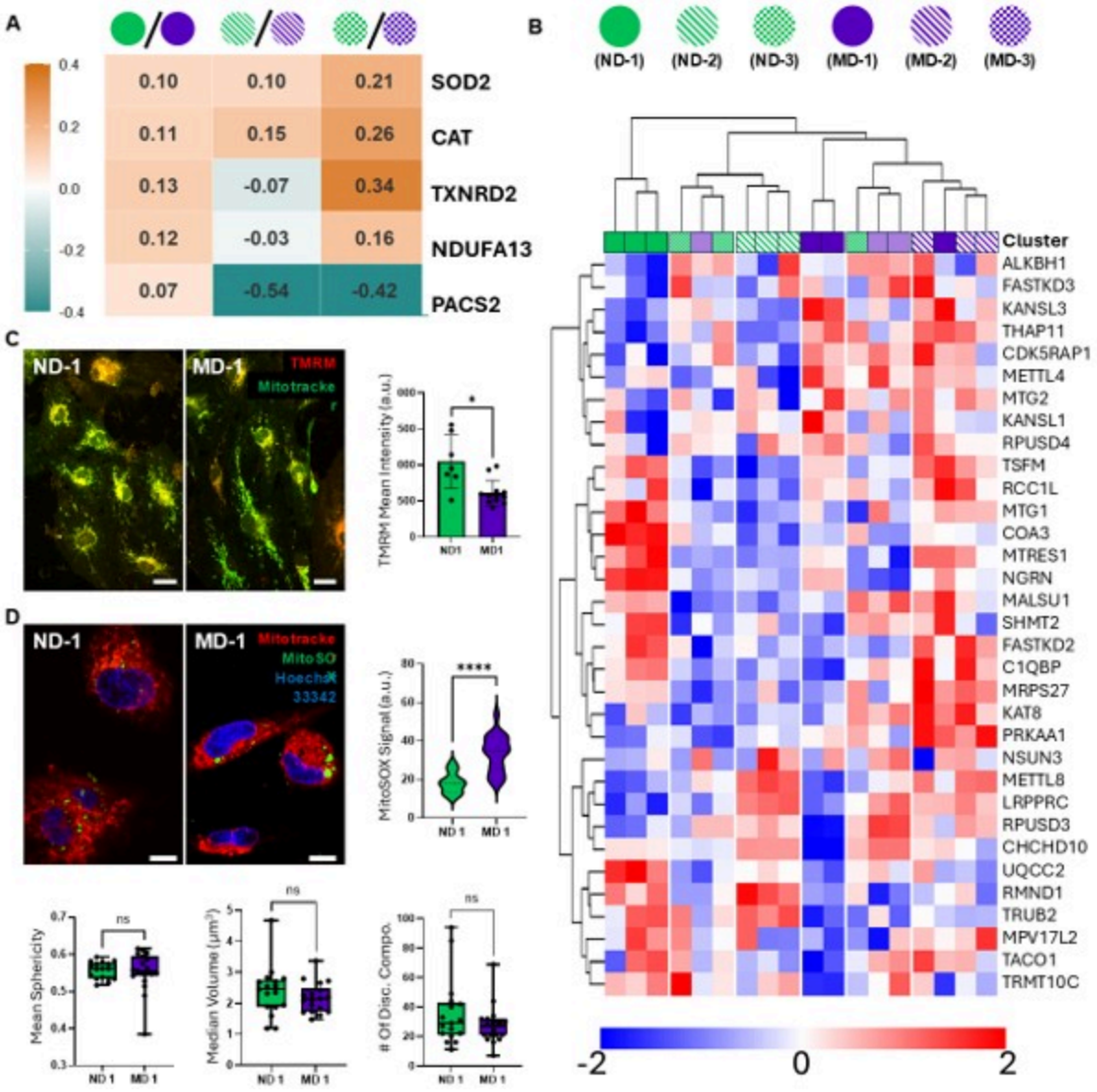



**Figure 4**

(A) Heatmap of mitochondrial regulation genes with associated DMRs. ND-hiPSC-EPs consistently show greater methylation in genes associated with reactive oxygen species handling. (B) Regulation of Mitochondrial Gene Expression shows separation between ND and MD lines. (C) TMRM signal from hiPSC-EPs ND-1 and MD-1. Representative images show an overlay of TMRM (Red) and Mitotracker (Green). Scalebar is 25 µm. Quantification shows lower overall mitochondrial polarization. N = 12 (MD-1) and N = 7 (ND-1) regions of interest. (D) Mitochondrial superoxide levels and mitochondrial morphology in hiPSC-EPs from ND-1 and MD-1. Representative images show MitoTracker (red), MitoSOX (green), and Hoechst 33342 (blue) Scalebar is 10 µm. Quantification demonstrates a significant increase in mitochondrial superoxide in MD-1 hiPSC-EPs, with no differences in the number of disconnected mitochondrial components, median mitochondrial volume or mean mitochondrial sphericity. N = 17 (ND-

1) and N = 19 (MD-1) unique cells from at least 4 separate regions of interest. Data are shown as mean ± SD. $p < 0.05$ (*) and $p < 0.0001$ (****). Comparisons made in (C) and (D) with two-tailed Student's T-test.

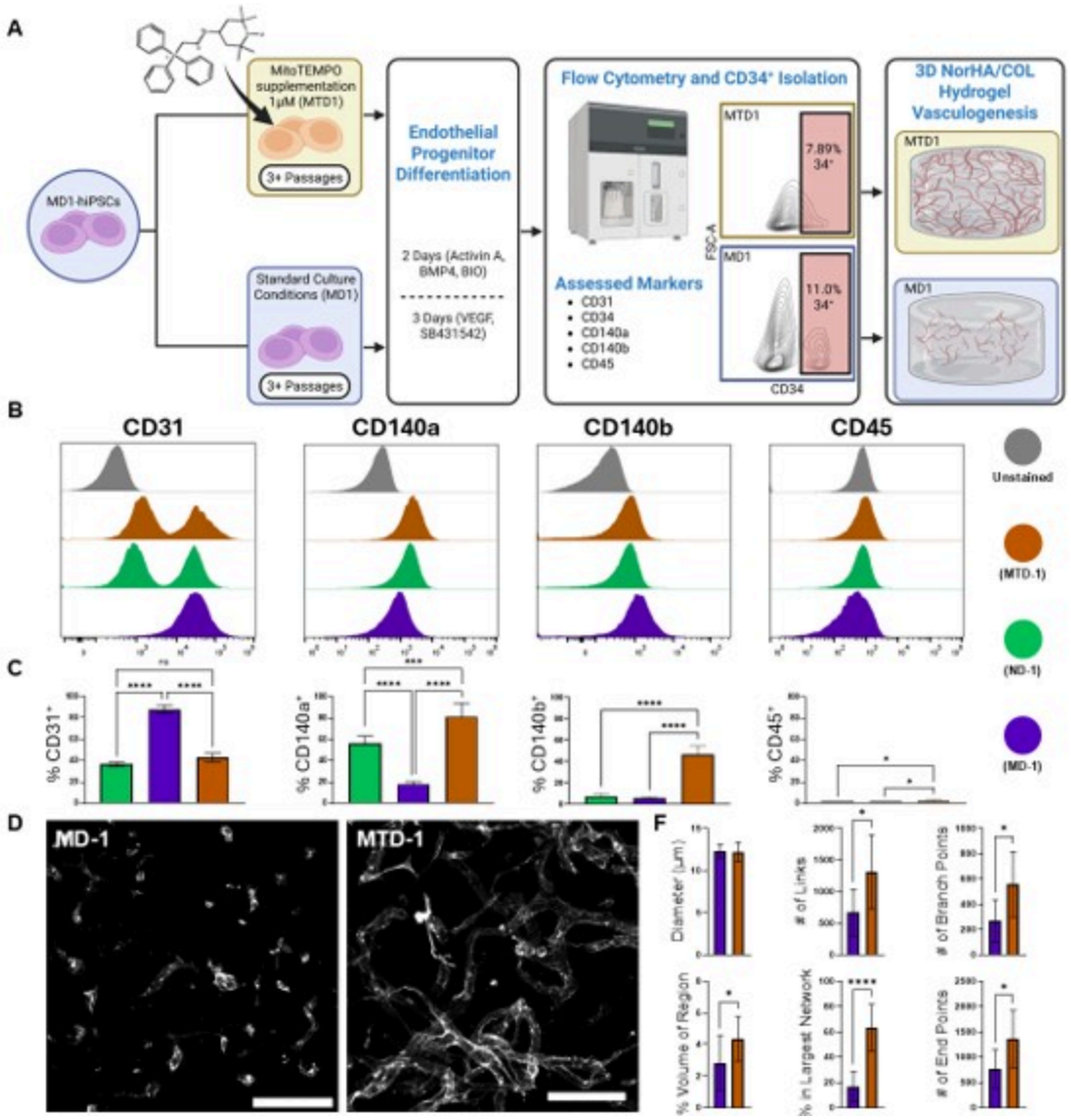



**Figure 5**

(A) Graphical abstract detailing the process of mitoTEMPO pretreatment and downstream analysis. (B) Modal histograms of $CD34^+$ cells assessed for CD140a, CD140b, and CD45 expression for ND1, MD1, and MTD1 hiPSC-EPs. (C) Relative percentage of $CD34^+$ cells co-expressing CD31, CD140a, CD140b and CD45. While all groups display a distinct CD31 population, ND1 and MTD1 show a dual population of $CD34^+$ only cells. Both ND1 and MD1 show an increase in CD140a; MTD1 additionally shows a CD140b-positive population. However, no distinct populations are observed for either marker, and no cell line shows CD45 expression. N = 3-6 independent differentiations. (D) Vasculogenic network formation in 3D Collagen/NorHA hydrogels. Representative z- projections depict network morphology of untreated MD-1 hiPSC-EPs (MD-1) and mitoTEMPO-treated MD-1 hiPSC-EPs (MTD-1). (F) Quantified network parameters show significant improvements in end points, volume of region, number of links, percent of cells incorporated in the largest network, and number of branch points following mitoTEMPO treatment.

N = 7 MD1; N= 16 MTD1 regions of interest; Scale Bar is 200 μm. Data are shown as mean ± SD. $p < 0.05$ (*), $p < 0.01$ (**), $p < 0.001$ (***), $p < 0.0001$ (****); Unshown comparisons are non-significant between matched pairs. Flow cytometry data in (A&C) were analyzed by one-way ANOVA with multiple comparisons. Vasculogenic network parameters in (D) were compared between MD1 and MTD1 using a two-tailed Student's t-test.

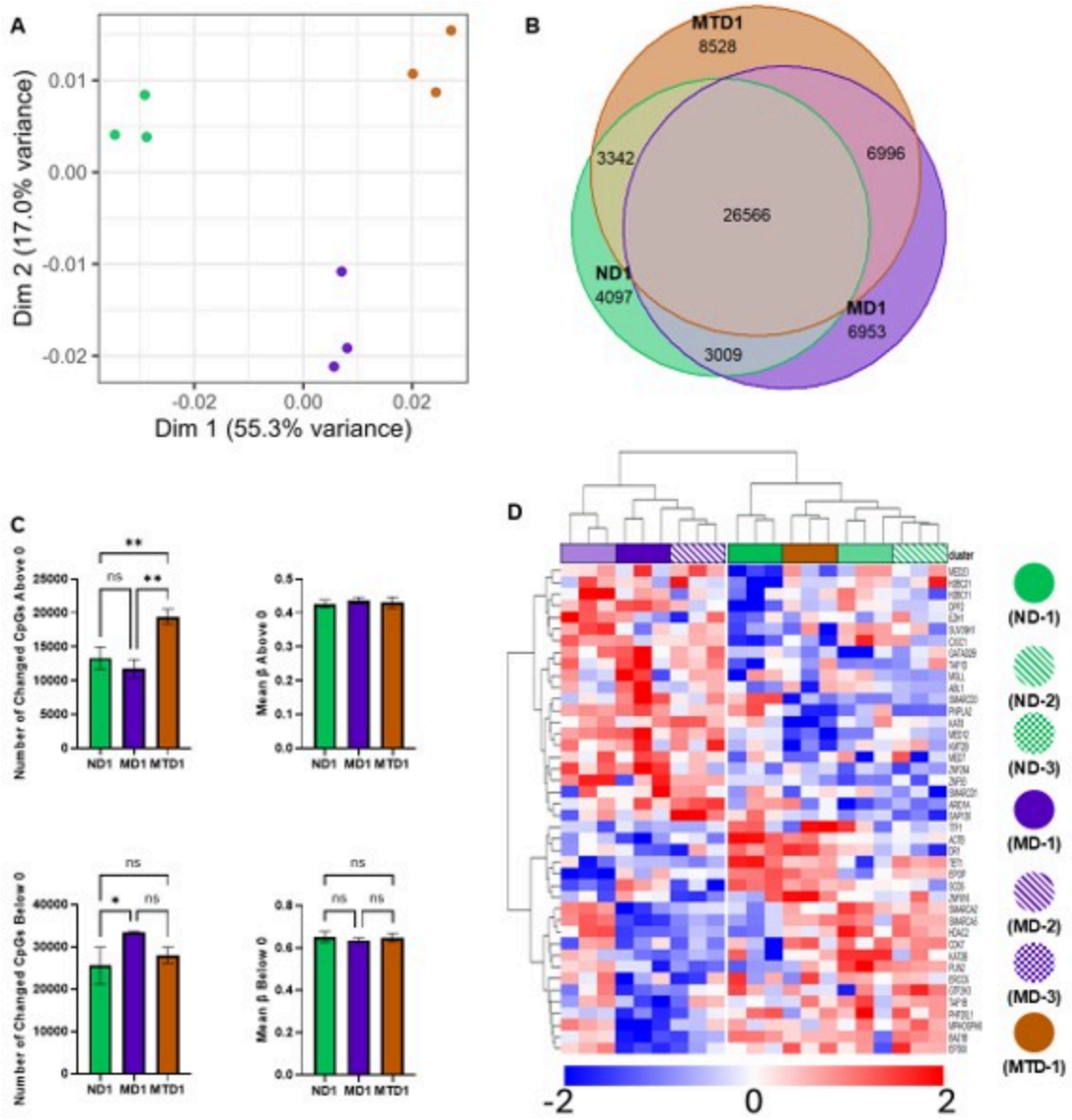



**Figure 6**

(A) MDS plot showing similarity between ND1- MD1 and MTD1 EPs, similar to grouping by age, MTD1 clusters with ND1 only in dimension 2 whereas in dimension 1 it clusters with MD1. (B) CpGs that showed a significant 15% magnitude difference between EPs and iPSCs. Shared changed CpGs represent the bulk of the Venn-diagram but each line shares unique CpG sites with every other line, including unique overlapping between ND1 and MTD1. (C) CpGs that showed a significant 15% magnitude difference between EPs and iPSCs and have an M score above 0. CpGs that showed a significant 15% magnitude difference between EPs and iPSCs and have an M score below 0. (D) Subset

of the pathway of Epigenetic Gene Regulation showing a split between ND and MD-hiPSCs with treated MD1-hiPSC-EPs grouping with ND-hiPSC-EPs. N = 3 independent differentiations. Data are shown as mean ± SD. $p < 0.05$ (*), $p < 0.01$ (**), $p < 0.001$ (***), $p < 0.0001$ (****); Unshown comparisons are non-significant between matched pairs.

## Supplementary Files

This is a list of supplementary files associated with this preprint. Click to download.

- SupplementalFigures.docx